Title: Olfactory microvillar tuft cells direct neurogenesis during allergic inflammation

Authors: Saltanat Ualiyeva[1] *, Evan Lemire[2] *, Amelia Boyd[1] *, Caitlin Wong[1] *, Evelyn C. Avilés[3], Alice Maxfield[4], Rachel Roditi[4], Ichiro Matsumoto[5], Nora A. Barrett[1], Kathleen M. Buchheit[1], Tanya M. Laidlaw[1], Joshua A. Boyce[1], Lora Bankova[1†] and Adam L. Haber.[2†]

Affiliations:

[1] Division of Allergy and Clinical Immunology, Jeff and Penny Vinik Center for Allergic Disease Research, Brigham & Women's Hospital and Department of Medicine, Harvard Medical School, Boston, MA.
[2] Department of Environmental Health, Harvard T.H. Chan School of Public Health, Boston, MA.
[3]Department of Neurobiology, Harvard Medical School, Boston, MA
[4]Division of Otolaryngology-Head and Neck Surgery, Brigham and Women's Hospital and Department of Otolaryngology-Head and Neck Surgery, Harvard Medical School, Boston, MA
[5]Monell Chemical Senses Center, Philadelphia, PA

* These authors contributed equally to this work
[†] Corresponding authors: ahaber@hsph.harvard.edu and lbankova@bwh.harvard.edu

Abstract: The olfactory neuroepithelium serves as a sensory organ for odors and a mucosal barrier which intimately interacts with the inhaled airstream. Odorant sensing is mediated by olfactory sensory neurons (OSNs), which along with diverse accessory epithelial cell types, are continuously replenished from a basal epithelial stem cell pool. This process of ongoing OSN differentiation is so far the only definitively established site of active adult neurogenesis in mice and humans. The mediators regulating the dynamics of this unique neurogenic niche are largely unknown and how olfactory neurogenesis is regulated by the environment is unclear. Here, integrating single-cell RNA sequencing and immunolocalization we define distinct markers of olfactory neuroepithelial cells, showing that *Muc2* uniquely identifies sustentacular cells and *Ncam1* is a robust mouse and human marker for OSNs. The enigmatic, transcriptionally uncharacterized subsets of olfactory microvillous cells (MVCs) correspond to nasal tuft cells and ionocytes in both mice and humans. Next we identify three morphologically, molecularly, and spatially distinct subsets of tuft cells: *Nrgn*$^{+}$ MVC, *Dclk1*$^{+}$ glandular and *Gnat3*$^{+}$ respiratory tuft cells. While distinct, these subsets of tuft cells share a core machinery for allergen recognition and generation of the eicosanoid mediators cysteinyl leukotrienes. Single-cell analysis of the response to inhaled allergens revealed robust induction of olfactory stem cell proliferation, which is abolished by tuft cell-specific deletion of *Ltc4s,* required for cysteinyl leukotriene generation. Together our data provide high resolution characterization of epithelial cell diversity in the nose, uncovering a novel mechanism by which the mucosal response to allergens, specifically tuft cell-derived eicosanoids, regulates stem cell proliferation in the olfactory neuroepithelium.

One Sentence Summary: We identify the functional role of enigmatic olfactory microvillous cells as regulators of olfactory remodeling in response to environmental signals.

Main Text: The nasal cavity is the first site of contact of inhaled air within the respiratory tract. It is divided by the septum into two air passages and an intricate system of turbinates and sinus cavities where the air is humidified, its temperature equilibrated to that of the lower airways and large particulate matter is trapped. The lining of the nasal cavity contains two functionally distinct mucosal compartments: respiratory epithelium and olfactory neuroepithelium, overlying a dense network of submucosal glands. Interspersed in both the respiratory and olfactory mucosa are immune cells, with increased density in the nasal-associated lymphoid tissue. Thus, the nose represents an extraordinary site of close interaction of epithelial cells, secretory glands, the immune and nervous systems (1).

The nasal respiratory epithelium shares the pseudostratified organization of the trachea with ciliated, secretory, basal cells and interspersed specialized epithelial cells. Immediately adjacent, the olfactory neuroepithelium is comprised of olfactory sensory neurons (OSNs) surrounded at the apical side by epithelial cells known as sustentacular "supporting" cells and microvillous cells (MVCs). Unique among neuronal tissues, the OSNs continuously regenerate from a population of proliferating epithelial stem cells called globose basal cells (GBCs). GBCs in turn derive from quiescent horizontal basal stem cells (HBCs), which also give rise to diverse olfactory epithelial cells. HBC activation and differentiation trajectories to epithelial cells and OSNs are defined at homeostasis and in the setting of profound chemical damage to the olfactory mucosa (2, 3). How physiologic environmental signals like allergens engage the olfactory epithelial cells to direct GBC and HBC proliferation and basal cell differentiation programs is still poorly characterized.

The majority of epithelial cells in the olfactory mucosa are termed sustentacular or supporting cells and are known for their phagocytic and detoxification function (4, 5). The less well defined olfactory MVCs consist of two distinct subsets (6), distinguished by the expression of the Transient Receptor Potential Cation Channel Subfamily M Member 5 (TRPM5), a taste receptor-linked calcium-activated monovalent cation channel (6). The TRPM5$^+$ MVCs are pear-shaped while the TRPM5$^-$ MVCs have a characteristic elongated shape (6, 7). Both TRPM5$^+$ and TRPM5$^-$ MVCs are derived from a common progenitor but differ in their differentiation trajectory (8). TRPM5$^-$ MVCs are defined by expression of the type 3 IP3 receptor (IP3R3) but lack TRPM5 and ChAT (6, 8, 9). TRPM5$^+$ MVCs express the acetylcholine-producing enzyme choline acetyltransferase (ChAT) (10-13). Futhermore, mice lacking TRPM5$^+$ MVCs exhibit disrupted olfactory behaviors in complex environments, suggestive of a role in regulating olfactory function (12). In addition, TRPM5$^+$ MVC-deficient mice have reduced proliferation of basal stem cells in the olfactory mucosa in the setting of chronic chitin exposure (14). Although this suggests a role for TRPM5$^+$ MVCs in directing olfactory basal cell proliferation, the specific MVC mediators and targets regulating olfactory neurogenesis have not been elucidated.

TRPM5 and ChAT notably also mark tuft cells, specialized cells in the trachea and intestine, as well as the nasal solitary chemosensory cell (SCC), which suggests shared activation pathways with the TRPM5$^+$ MVC (10, 15-20). Tuft cells are distinguished by the expression of members of the taste receptor type I and II families as well as the taste signaling G protein Gα gustducin encoded by *Gnat3* (19, 21, 22) (20, 23). Tuft cells are also the dominant source of IL-25, an important initiator of mucosal type 2 immune responses (17, 23-26). Airway tuft cells are direct sensors of allergens and the danger signal ATP, which trigger the generation of pro-inflammatory lipid mediators, specifically cysteinyl leukotrienes (CysLTs), and can direct both immune mediated and direct epithelial remodeling after allergen sensing (27, 28).

Despite their common expression of ChAT and TRPM5 with tuft cells and nasal SCCs, olfactory MVCs are considered a distinct cell type. They have very low to absent expression of taste receptors and Gα gustducin (29), and only rare contact with sensory neurons (6, 7), a defining feature of both nasal SCCs and tracheal tuft cells (30, 31). Olfactory MVCs are also smaller and pear-shaped unlike the spindle-shaped nasal respiratory SCCs and tracheal tuft cells (10). Yet, MVC development depends on Pou2f3, a transcription factor required for tuft cell development (29, 32, 33). Thus, TRPM5$^+$ MVCs share origin and activation machinery with the rest of the chemosensory family. However, if TRPM5$^+$ MVCs possess the full mediator capacity of tuft cells and how they direct allergen-induced olfactory neuroepithelial remodeling is not known.

Here, we used ChAT-eGFP mice to enrich MVCs from the olfactory and SCCs from the respiratory epithelium for single-cell RNA-sequencing (scRNAseq) analysis demonstrating that MVCs, SCCs and a third "intermediate" population of ChAT-eGFP$^+$ nasal epithelial cells all belong to the tuft cell family. Although each population can be defined by unique markers, they share a core transcriptional profile including *Trpm5, Pou2f3, Chat, Avil* and *Ltc4s*. The transcriptionally distinct population of TRPM5$^-$ MVCs shares multiple features with tracheal ionocytes (*Cftr, Foxi1, Ascl3, Coch*). We applied supervised machine learning approaches to accurately assess the transcriptome-wide similarity of detected cell-types to known subtypes in the trachea, which confirmed the identity of TRPM5$^+$ MVCs as tuft cells, and of TRPM5$^-$ MVCs as ionocytes. We assembled the largest single-cell atlas of the mouse nasal mucosa (containing 63,125 cells) including analysis of the response to inhaled mold allergens. We found that allergen inhalation caused a marked proliferation of HBCs in the olfactory mucosa, even in the absence of profound damage to the OSNs or accessory epithelial cells. Strikingly, this allergen-induced stem cell proliferation was abolished by genetic deletion of cysteinyl leukotriene production in tuft cells using Chat^{Cre} mediated deletion of *Ltc4s*, demonstrating that eicosanoid production by tuft cells is critical for olfactory regeneration. Taken together, our data define extensive heterogeneity of rare sensory epithelial cell-types in the nasal mucosa and define the functional consequences of their effector programs for olfactory neurogenesis.

Results: First, to define the distribution of mouse olfactory and respiratory nasal chemosensory ChAT-eGFP$^+$ cells by flow cytometry (FACS), we separated olfactory from respiratory mucosa along the anterior portion of the olfactory turbinates and obtained single-cell suspensions from each compartment (**Fig. S1A**). As expected, the olfactory mucosa contained the majority of ChAT-eGFP$^+$ cells (11) (69%) compared to 31% derived from the respiratory mucosa (**Fig. S1B-F**). ChAT-eGFP$^+$ cells were abundant in the olfactory mucosa (22 % of EpCAM^{high} cells and 2% of live cells) but were also surprisingly prevalent in the respiratory mucosa (10% of EpCAM^{high} cells and 1% of live cells) (**Fig. S1B-E**). Our previous bulk RNA-seq data demonstrated flow cytometric identification of globular MVCs (FSC/SSC^{low}) and elongated SCCs (FSC/SSC^{high}) and showed both are ChAT-eGFP positive (27). Surprisingly, here we found that the olfactory and respiratory mucosa had similar distribution of globular vs elongated ChAT-eGFP$^+$ cells suggesting that the abundant MVCs, previously described exclusively in the olfactory mucosa, might also be found in the respiratory epithelium albeit in lower numbers (**Fig. S1G, H**). Elongated ChAT-eGFP$^+$ cells were also found in both respiratory and olfactory mucosa. They were extremely rare in both locations accounting for <500 cells/mouse (**Fig. S1H**).

TRPM5⁺ and TRPM5⁻ MVCs correspond to tuft cells and ionocytes respectively.
To characterize the subsets of nasal ChAT-eGFP⁺ cells transcriptionally, we compared the ChAT-eGFP⁺ cells to EpCAM^{high} nasal epithelial cells from each of olfactory and respiratory epithelia by scRNAseq (**Fig. 1A** and **Fig. S1A**). To ensure sufficient SCC cell numbers for transcriptional analysis, we enriched for the scarce elongated ChAT-eGFP⁺ cells so they represented one third of the cells submitted for scRNAseq, while another third was the ChAT-eGFP⁺ globular cells and the remainder were EpCAM^{high} GFP⁻ cells (**Fig. S1I)**. Dimensionality reduction and unsupervised clustering (**Methods**) identified a subset of cells defined by known tuft cell markers (**Table S1** and **S2**) that clustered distinctly from all other EpCAM^{high} cells from the respiratory and olfactory mucosa (**Fig. 1A**). Transcriptome-wide machine learning analysis confirmed that these are indeed highly similar to tracheal tuft cells, with 94% of the cells in the TRPM5⁺ MVC cluster being classified as tuft cells by a random forest classifier trained on previously published single-cell data from the tracheal epithelium (22) (**Methods**, **Fig. 1B**). Besides tuft cells, we identified a second population of differentiated epithelial cells negative for *Chat* and *Trpm5* but positive for *Itpr3* and *Ascl3*, consistent with descriptions of TRPM5⁻ MVCs (8, 9, 34). These cells expressed high levels of *Cftr, Coch* and *Foxi1*, and the random forest mapped 96% to tracheal ionocytes (**Fig. 1B**), unambiguously identifying them as nasal ionocytes (**Fig. 1B)**.

Although both tuft cells and ionocytes still represent a minority of epithelial cells, they appeared markedly more abundant in the nose than their reported concentration in the trachea (22). To characterize their actual distribution in the nose, we evaluated the numbers of tuft cells and ionocytes in a non-enriched scRNAseq dataset from the nose (to be introduced in **Fig. 4**) and compared to published tracheal scRNAseq data (22). Examining this non-enriched dataset, we found that tuft cells comprise 5.1% (95% CI: 4.9-5.7) of EpCAM⁺ cells from the olfactory epithelium, 2.7-fold more common than in the trachea (**Fig. 1C)**. Ionocytes comprise 5.6% (95% CI: 5.3-6.5) of EpCAM⁺ cells from the olfactory epithelium, 2.7-fold more common than in the trachea (**Fig. 1C**). Nasal tuft cells were defined by the expression of the canonical markers defined by our previous scRNAseq analyses of the trachea and intestine: the taste transduction channel *Trpm5,* Ca^{2+}-regulated actin-binding protein *Avil,* and eicosanoid biosynthetic enzymes *Alox5ap* and *Ltc4s* (**Fig. 1D**). Immunofluorescence of cross sections of nasal mucosa confirmed that both cochlin⁺ and CFTR⁺ ionocytes and ChAT-eGFP⁺ tuft cells are abundant in the olfactory mucosa (**Fig. 1E)** and ionocytes are found in lower numbers in the respiratory epithelium (**Fig. S2A**). The remainder of the EpCAM^{high} cells comprised of differentiated epithelial cells, basal cells, and olfactory major protein (OMP) expressing sensory neurons (**Fig. 1A**). As expected, we found that the majority of OMP⁺ neurons are derived from the olfactory mucosa (**Fig. S2B**) and thus represent OSNs. A second distinct population of olfactory neurons was derived from the respiratory mucosa and were positive for aquaporin 4 (**Fig. S2B-E**), a distinguishing marker between olfactory and vomeronasal neurons in rodents (35) validating our separation of tissue origin and identifying these cells as vomeronasal sensory neurons (VSNs).

TRPM5⁺/ChAT⁺ cells in the olfactory and respiratory mucosa of the nose are historically defined as distinct epithelial subsets – olfactory MVCs and respiratory SCCs, largely based on the absence of taste receptors and transduction machinery in MVCs (7, 10, 36). However, we find that *Trpm5*⁺/ChAT⁺ cells derived from both the olfactory and respiratory mucosa share a core transcriptional profile defined by transcripts involved in taste transduction (*Trpm5*, *Gng13*), multiple calcium signaling molecules (*Pik3cg, Hck, Vav1, Matk, Pik3r5*), the transcription factors *Spib* and *Pou2f3* and the cysteinyl leukotriene (CysLT) biosynthetic enzymes *Alox5,*

Alox5ap and *Ltc4s* (**Fig. 1F**). This core effector profile is shared by tuft cells in the trachea (22) and intestine (23) defined by our previous single-cell analysis (**Fig. 1G**). Thus, tuft cells in all mucosal compartments are distinguished by the expression of the necessary machinery to rapidly generate Ca^{2+} dependent mediators.

To confirm the capacity of nasal tuft cells to generate CysLTs, we stimulated sorted ChAT-eGFP^{+} cells from the nasal mucosa *ex vivo* with Ca^{2+} ionophore or ATP and assessed the supernatants for generation of LTC_4 and LTC_4 metabolites LTD_4 and LTE_4 by liquid chromatography/mass spectrometry (LC-MS). Tuft cells generated high levels of LTC_4 with minimal levels of the conversion product LTE_4 and no LTD_4 detected in the supernatant by LC-MS (**Fig. 1H, I**). Our data therefore indicate that *Trpm5*$^{+}$/*Chat*$^{+}$ nasal tuft cells share not just a common transcriptional origin (Pou2f3), but importantly a core effector potential that allows them to rapidly respond to luminal signals through Ca^{2+} flux and generation of potent lipid mediators.

Three subsets of nasal tuft cells correspond to MVCs, SCCs and a new population of intermediate tuft cells.

Our scRNAseq evaluation demonstrated that all *Chat*$^{+}$*Trpm5*$^{+}$ nasal epithelial cells share the tuft cell transcriptional profile. To reconcile this data with the literature that defined olfactory MVCs as distinct from respiratory SCCs and other chemosensory cells, we next sought to dissect their heterogeneity at the single-cell level. We found three subclusters of tuft cells (**Fig. 2A**) and defined the unique markers of each cluster by differential expression analysis (**Fig. 2B, Table S3**). To place each nasal chemosensory subset within the tuft cell family, we assessed the expression of the pan tuft cell signature by Nadjsombati *et al*. in each subset (37) (**Fig. S3A**). We then compared each subset to the tracheal tuft cell subsets (5) using a machine learning algorithm, random forest classifier (**Fig. 2C**). We sorted elongated (FSC^{high}) and globular (FSC^{low}) tuft cells from the olfactory and respiratory epithelium for bulk RNAseq (**Fig. S3B, C, E, F**). We applied a support-vector machine regression deconvolution approach CIBERSORTx (38) to infer the proportions of our newly defined tuft cell subsets within the sorted samples and confirm their distribution and morphology (**Fig. S3H**). Finally, we performed spatial immunophenotyping throughout the nasal mucosa to definitively localize and characterize the tuft cell subsets and markers uncovered by scRNAseq (**Fig. 2E-O**).

The dominant population of tuft cells in the nose was largely derived from the olfactory mucosa (**Fig. 2A** and **S3B, C**). These cells were characterized by the high expression of the cyclooxygenase enzyme *Ptgs1* and the tuft cell cytokine *Il25* identified by scRNAseq (**Fig. 2B**). These olfactory tuft cells were also positive for *Pou2f3, Trpm5* and *Chat* (**Fig. S3D** and **S3I**), the original markers of MVCs (6, 7, 11, 29) as well as the pan-tuft cell marker *Avil* and had low expression of the taste receptor-associated G proteins *Gnat3* and *Gnb3* (**Fig. S3I**). When we compared their expression profile to the pan-tuft cell signature we found them to express a high proportion of tuft cell-specific genes (**Fig. S3A**). Specifically, besides *Ptgs1* and *Il25,* they express the eicosanoid biosynthetic enzymes *Hpgds, Alox5ap, Alox5* and *Ltc4s* (**Fig. S3G**). In whole mounts of the olfactory mucosa, we found abundant ChAT-eGFP^{+} cells with globular body and a single very short process ending with short brushes at the apical surface, identical to the morphology of MVCs (**Fig. S3E, F**). Thus, we refer to these small, globular *Chat*$^{+}$*Trpm5*$^{+}$ cells that lack expression of taste receptors and share the tuft cell signature as tuft-MVCs.

We then compared the tuft-MVCs to the tracheal scRNAseq defined tuft cell subsets and found that tuft-MVCs are most similar to the eicosanoid-enriched tuft-2 cells (**Fig. 2C**).

Deconvolution analysis (Methods) of bulk RNAseq of tuft cells sorted based on morphologic characteristics confirmed that tuft-MVCs represent the majority of the FACS-defined globular (FSC^{low}) nasal ChAT-eGFP^{+}cells (**Fig S3H**). Finally, we identified a new marker of tuft-MVCs, *Nrgn* encoding neurogranin, a postsynaptic neuronal protein in the calpacitin family that preferentially binds to the Ca^{2+}-free form of calmodulin (39) (**Fig. 2B, D**).

A second distinct but very rare population of tuft cells were derived exclusively from the respiratory epithelium (**Fig. 2A** and **S3A, S3B**). These cells were enriched for transcripts that define the elongated nasal respiratory SCCs, including type 1 (*Tas1r1*, *Tas1r3*) and type 2 (*Tas2r104*, *Tas2r105*, *Tas2r108*, *Tas2r118*, and *Tas2r138*) taste receptors, and the taste signaling molecules *Gnat3* and *Gnb3* (18, 30, 40-43) (**Fig. 2B**). As expected, the rare respiratory tuft cells have a spindle-shaped morphology (**Fig. S3E**). Comparison to the pan-tuft transcriptional signature demonstrated that the spindle-shaped tuft cells are also enriched for the core tuft cell genes (**Fig. S3A, G, I**). Because of their characteristic spindle-shaped morphology and marker expression consistent with that of the SCCs combined with the transcriptional profile of tuft cells, we refer to them as tuft-SCCs. The tuft-SCCs are most similar to the taste receptor-enriched tracheal tuft-1 with 68% classified as tuft-1 (**Fig. 2C**). Further deconvolution analysis (Methods) revealed that their transcriptome closely resembled that of FACS defined rare respiratory elongated (FSC^{high}) ChAT-eGFP cells (**Fig. S3H**).

Finally, we identified an intermediate population of tuft cells that shared features with both tuft-MVC and tuft-SCCs yet appeared distinct (**Fig. 2A**). Highlighting their intermediate character was the distribution of *Nrgn, Gnb3,* and *Gnat3* markers specific to tuft-MVC and tuft-SCC, which were moderately expressed (**Fig. S3I**). Comparison to the pan-tuft cell signature demonstrated they were the most highly enriched among the nasal tuft subsets for the pan-tuft cell genes (**Fig. S3A, G, I**). This subset expressed the highest level among the nasal tuft cells of *Il13ra1*, which is responsible for tuft cell proliferation in the intestine in the setting of type 2 inflammation (44). Consistent with that, they were most similar to the tuft cell progenitor population in the trachea (**Fig. 2C**). Analysis of our morphology based bulk RNAseq data strongly suggested that these cells were equally represented in the bulk RNAseq subsets of elongated (FSC^{high}) and globular tuft cells (FSC^{low}) and likely of intermediate morphology (**Fig. S3H**). Interestingly, among the transcripts that distinguish the intermediate population of tuft cells were *Ly6d* and *Ly6e,* transcripts associated with breast and prostate glandular cancers (45-47) (**Table S3**). Thus, and in addition due to their anatomical location in the lateral nasal gland (see below) we refer to them as tuft-gland.

We then set out to define the distinguishing markers of the three nasal tuft cell subsets. Tuft-MVCs are defined by the high and ubiquitous expression of *Nrgn*, *Pou2f3, Avil* and lack of taste receptors and signaling molecules (**Fig. 2B, D**, **S3D, S3I**). Notably, tuft-MVCs had very low levels of expression of *Dclk1,* a marker used for identification of tuft cells in the intestine and trachea (25, 26, 48) (**Fig. 2D** and **S3I).** The tuft-SCCs were negative for *Nrgn*, high for the taste transduction Gα gustducin gene *Gnat3* and had low expression of *Dclk1* (**Fig. 2B, D** and **S3I**). Finally, *Dclk1,* low in tuft-MVCs or tuft-SCCs, was highly expressed in the intermediate population tuft-gland cells (**Fig. 2D** and **S3I**). Tuft-SCCs were the exclusive source of the neuropeptide bone-derived neurotrophic factor (*Bdnf*) and the cytokine *Il10* at homeostasis (**Fig. 2B**) suggesting a possible immunomodulatory role. Although *Il25* expression was shared among all tuft cells, its expression was 1.8-fold higher in tuft-MVCs than the intermediate tuft population, and ~6 fold higher than the tuft-SCC population (**Fig. 2B** and **S3G**). We find all tuft cell subtypes express receptors for norepinephrine, but specific receptors are distinct in each

group – beta-2-adrenergic receptor (*Adrb2*), alpha-2-adrenergic receptor (*Adra2a*), beta-1 adrenergic receptor (*Adrb1)* in the tuft-MVC, tuft-gland, and tuft-SCC respectively – raising the intriguing possibility of distinct interactions with norepinephrine secreting sympathetic neurons (49) (**Fig. 2B**).

Having identified several transcriptional markers that distinguish the three nasal tuft cell subsets, we set out to define their distribution in the nasal mucosa using immunofluorescence within the different spatial compartments of the nose. Using neurogranin as a tuft-MVC marker, we found a distinct population of neurogranin-positive cells predominantly in the olfactory mucosa but also notably present, albeit less abundant in the respiratory mucosa (**Fig. 2E**). This newly appreciated distribution of tuft-MVCs outside the olfactory mucosa was consistent with our FACS and scRNA-seq data suggesting that globular cells with MVC transcriptional characteristics are not restricted to the olfactory mucosa (**Fig. S1C, G, H** and **S3B, C, H**) and account for the highest proportion of tuft cells in the respiratory mucosa (**Fig. S1G, H**). Tuft-MVCs are ChAT-eGFP^{+} and positive for the pan-tuft cell marker advillin (**Fig. 2F-H**). Conversely, neurogranin and Gα-gustducin marked distinct cellular subsets in the respiratory epithelium (**Fig. 2L**, **Fig. S4C, D, F**). We confirmed that the olfactory and respiratory neurogranin^{+} cells are absent in tuft cell-deficient *Pou2f3*$^{-/-}$ mice validating neurogranin as a true tuft cell marker (**Fig. S4A-B**). Thus, neurogranin is a specific marker for tuft-MVCs in the respiratory and olfactory mucosa and tuft cells with the transcriptional and compositional makeup of olfactory MVCs are distributed throughout the olfactory and respiratory mucosa.

We found a separate distinct population of tuft cells in the lateral nasal gland – a large serous glandular structure unique to the nasal cavity (**Fig. 2I**). These tuft cells were positive for the pan-tuft cell markers ChAT and advillin but also positive for neurogranin, Gα-gustducin and DCLK1, suggesting that they correspond to the intermediate population of tuft-gland cells (**Fig. 2I, J** and **S4E, G**). Tuft-SCCs as expected were found in the respiratory epithelium exclusively and were marked by ChAT, advillin and Gα-gustducin (**Fig. 2K, L**). Finally, we characterized the vomeronasal organ (VNO) ChAT-eGFP^{+} cells as positive for Gα-gustducin (41) but negative for neurogranin and DCLK1 making them most similar to tuft-SCC despite their location surrounded by OMP expressing neurons (**Fig. S4H-J**). Notably, DCLK1 also marked epithelial cells with ductal morphology in the olfactory mucosa (**Fig. 2I**). Lastly, we used *in situ* hybridization to define the distribution of *Ltc4s* mRNA in the nasal mucosa. *Ltc4s* mRNA was ubiquitously found in all subsets of nasal tuft cells including tuft-MVCs in the olfactory mucosa (**Fig. 2M**), tuft-gland in the lateral nasal gland (**Fig. 2N**) and tuft-SCCs in the respiratory epithelium (**Fig. 2O**) confirming that *Ltc4s* is broadly expressed in all subsets of tuft cells.

Human microvillar cells are tuft cells and ionocytes which express canonical markers

Having characterized the subsets of respiratory and olfactory mouse nasal tuft cells, we sought to determine if their profile and distribution is mirrored in the human nose. We reanalyzed existing scRNAseq datasets and immunophenotyped nasal samples from the respiratory and olfactory mucosa. Human SCCs in the respiratory epithelium share many of the reported features of mouse SCCs including taste receptors and IL-25 expression, and their numbers are higher in patients with fungal and chronic rhinosinusitis compared to healthy controls (50-52). To define the human SCC transcriptional profile, we reanalyzed scRNAseq profiles of nasal epithelial cells derived from sinus surgeries of patients with chronic rhinosinusitis with or without polyposis (**Fig. 3A, 3B, Table S4, Methods**)(53) and confirmed that 13 of the 19,196 cells profiled are indeed nasal tuft cells. They were identifiable by their specific expression of pan-tuft cell markers *LRMP, RGS13*,

AVIL (**Fig. 1F**), taste transduction proteins *TAS1R3* and *PLCB2*, and the IL-25 receptor (*IL17RB*). We found rare DCLK1$^+$ spindle shaped cells in respiratory epithelium of ethmoid sinus and superior turbinates derived from patients (*n*=3) with chronic rhinosinusitis (**Fig. 3C**) and confirmed that advillin is a reliable marker of both mouse and human tuft cells (**Fig. 3D**).

Human microvillar cells are described by anatomical studies of olfactory mucosa, but it is not known if these elongated cells represent tuft cells, ionocytes or both (54, 55). To determine if human MVCs share the features of mouse MVCs, we reanalyzed a recent dataset of human olfactory mucosa by Durante *et al* (56). Focused analysis of a cluster of 116 MVCs identified two subsets (**Fig. 3E**), and differential expression analysis identified a subset of human MVCs with highly similar transcriptional makeup to mouse tuft-MVCs with distinct expression of eicosanoid pathway components *ALOX5AP* and *PTGS1,* the IL-25 receptor *IL17RB* and the pan-tuft cell marker *AVIL* (**Fig. 3F**).

We then set out to determine how olfactory human microvillar relate to mouse MVCs. To reliably identify human olfactory epithelium in biopsies, we first aimed to identify markers beyond olfactory receptors and OMP of human OSNs. Leveraging scRNAseq, we discovered that *NCAM1* is a specific marker expressed at high levels in both mature and immature human OSNs while *OMP* is a specific but not highly expressed mature OSN marker **(Fig. S4K**). To verify NCAM1 as an olfactory marker, we examined healthy sinonasal mucosa resected during trans-sphenoidal surgery from 3 patients. We found that NCAM1 clearly marks human olfactory neuroepithelium including the axons of mature OSNs in proximity to OMP$^+$ OSNs (**Fig. 3G**). In the olfactory neuroepithelium, advillin$^+$ cells with the globular morphology of olfactory tuft-MVCs were interspersed in the olfactory mucosa suggesting a shared morphology and distribution with mouse tuft-MVCs (**Fig. 3G**). Finally, we confirmed that human tuft-MVC express *Alox5, Alox5ap,* and *Ltc4s*, allowing them to generate CysLTs (**Fig. S4K**) providing a clear functional connection to mouse tuft-MVCs.

In addition to tuft cells, our re-analysis of scRNAseq data also identified a cluster of 79 ionocytes in the human respiratory epithelium (**Fig. 3A, 3B**) and 86 ionocytes in the olfactory enriched human mucosa (**Fig. 3E, 3F**). The human nasal ionocytes shared the transcriptional profile of human pulmonary ionocytes and mouse pulmonary and nasal ionocytes with unique expression of the ion channels *CFTR*, *CLCNKB*, the transcription factors *FOXI1* and *ASCL3*, and the vacuolar ATP-ase *ATP6V1B1*. We validated the presence of ionocytes in human respiratory and olfactory nasal tissue using expression of FOXI1 (**Fig. 3H**, **I**).

In summary, we confirmed that the human tuft cells and ionocytes represent two distinct subsets of the previously described human MVCs in the olfactory mucosa. Human tuft cells are heterogeneous in the nose similar to mouse tuft-MVCs and tuft-SCCs but share a core transcriptome. Ionocytes, a more homogenous population of specialized epithelial cells, are found in the olfactory mucosa as expected, but also in high numbers in the respiratory mucosa.

Characterization of the mouse nasal mucosal immune system

As we and others have shown, tuft cells are epithelial sensors that regulate local immunity (57). We therefore sought to comprehensively profile the nasal mucosal immune system at homeostasis and its response to inhaled allergens to enable mapping the downstream targets of tuft cell effector molecules. We performed scRNA-seq at homeostasis (**Fig. 4A,** left) and after nasal inhalation of the mold allergen *Alternaria alternata* (**Fig. 4A,** right panels) in the innate phase (36 hours after a single inhalation) and adaptive phase (36 hours after 2 inhalations given 6 days apart). We included equal numbers of EpCAM$^+$ epithelial cells expanding the gating strategy to include EpCAM high

and intermediate/OSNs and CD45$^+$ immune cells, and again used microdissection to sample cells from olfactory and respiratory mucosa. *Alternaria* elicits strong innate and adaptive immune responses in the airways (26, 28, 58-60) initiated by the activation of several epithelial subsets including tuft cells, which respond by generating CysLTs (27). In total we profiled 50,448 high-quality cells after filtering (**Methods**). Unsupervised cluster analysis (**Methods**) detected 11 subtypes of myeloid (**Fig. S5A, B)** and 17 subtypes of lymphoid cells (**Fig. S5C, D**).

At homeostasis, in the myeloid compartment, the major clusters of cells were dendritic cells, macrophages and monocytes as expected (**Fig. 4B**), but we also observed a substantial fraction of tissue-resident neutrophils (11.7%), along with eosinophils (4.3%), basophils (0.4%), and mast cells (0.1%), osteoclasts (0.3%) and a *Kit*$^+$*/Cd34*$^+$ subset which likely represents common myeloid progenitors (CMP, 4.9%). Cell fractions assayed using FACS largely recapitulated the composition estimates from the single-cell data, particularly the surprisingly high fraction of neutrophils in the naïve nasal mucosa (**Fig. 4C**). In the lymphoid compartment, we identified all three previously described innate lymphoid cell (ILC) subsets. The ILC2 subset accounted for 5 and 6% of the hematopoietic cell pool in the olfactory and respiratory epithelia respectively (**Fig. S6A, Table S9**). We recovered all canonical T helper subsets except for T_H1 cells and observed a population of γδ T cells which expressed high levels of *Il17a* and *Rorc* (**Fig. S5D**) as did T_H17 cells. Both *Il17a*-expressing subsets were significantly enriched in the respiratory epithelium (**Fig. S6A, B**), as were γδ T cells, ILC1, and NK cells (**Fig. S6B**).

Inference of intercellular communication identifies targets of tuft cell mediators

Downstream of sensing of airway contents by surface receptors, information is transduced via intercellular signals encoded by proteins and bioactive lipids, most notably the eicosanoid family. Tuft cells, which produce several pro-inflammatory lipid mediators: CysLTs (**Fig. 1H, I**), the pro-inflammatory prostaglandin PGD_2 and low levels of the immunomodulatory prostaglandin PGE_2 (**Fig. S6C, D**) (27, 28), feature prominently in these signaling cascades. We defined literature-curated enzymatic pathways required for synthesis of a range of eicosanoids (**Fig. S5F, Table S5**), to identify each cell-type capable of synthesizing each small molecule (**Methods**). As expected, we found that tuft cells, and particularly the tuft-MVC subset, produce abundant enzymes required for synthesis of LTC_4, PGD_2, PGE_2, and also PGF_2 and PGJ_2 (**Fig. S5G**). We mapped out their cellular targets by testing for expression of the cognate receptors for each lipid (**Fig. 4D, Methods**), confirming that CysLT receptors *Cysltr1* and *Cysltr2* are expressed by ILC2s in the nose, as well as in dendritic cells and macrophages, similar to their expression in the intestine (61) and lung (62-65). Surprisingly, we noted that *Cystlr1* was also expressed by the epithelial neural precursors GBCs (**Fig. 4D**) and HBCs (**Fig. S5G**). *Cysltr2* was expressed by olfactory ensheathing glial cells (**Fig. 4D**). The major site of expression of the PGD_2 receptor DP1 (*Ptgdr)* is in epithelial cells and largely absent in immune cells. This might explain the function of PGD_2 as a potent secretagogue in the nasal cavity (66). The second PGD_2 receptor CRTH2 (*Ptgdr2*) was not detected in any of the populations we assessed. We did not detect *Cysltr3* in epithelial cells or immune cells in the nose, which is largely consistent with the low level of mRNA expression of the third CysLT receptor (26, 67).

Inflammatory response to aeroallergen inhalation in the nasal mucosa

In the immune compartment the initial response 1 day after a single inhalation of *Alternaria* allergen, revealed relatively stable numbers of immune cell subsets, except for a 43.0% [CI-95: 12.3, 62.9] decrease in macrophage numbers (**Fig. 4E**). During the adaptive phase of inflammation

36 hours after the second of 2 doses of *Alternaria* **(Fig. S5E)**, we observed increased number of polarized T cells, particularly a 1.9-fold [CI-95: 0.87, 4.3] increase in activated T_H2 cells as expected, but also a 2.1-fold [CI-95: 1.03, 4.42] increase in regulatory T (T_{reg}) cells. Concomitant with the increase in adaptive lymphocytes, we observed a marked reduction in almost all myeloid cell numbers (**Fig. 4E** and **Table S9**).

We defined cell-type specific genes (**Table S6**) and performed differential expression (DE) analysis (**Fig. S6E-F**, **Methods**), which showed that *Alternaria* drove a type 2-polarized innate immune response 24 hours after inhalation with type 2 effector cytokines *Il5* (FDR=0.007) and *Il13* (FDR=0.302) specifically upregulated by ILC2s (**Table S7**). Type 2 helper T (T_H2) cells showed the strongest transcriptional response to a second *Alternaria* dose (**Fig. S6E)**. We additionally observed up-regulation of *Ltc4s* in dendritic cells, eosinophils and tuft-MVCs (all FDR<0.25, **Table S7**), consistent with increased production of CysLTs – including by tuft cells – as part of the early innate inflammatory response. We characterized the intercellular signaling induced by the aeroallergen among the diverse cell types of the nasal mucosa (**Fig. 4F**). Following the approach we previously developed (68), we mapped all receptor-ligand gene pairs – annotated in either CellPhoneDB 2.0 (69) or the FANTOM5 (70) databases – which showed differential expression in response to *Alternaria* (**Methods, Table S8**). In addition to the classical cytokines *Il5* and *Il13*, additional effector signaling associated with type 2 inflammation was upregulated by ILC2s including *Calca,* (**Fig. 4F**) and *Il17rb* (**Table S7**). Consistent with this type 2 polarization, the activation receptor *Ilr2a* on T_H2 cells was up regulated, while the NK and ILC1 chemoattractant *Ccl4* (associated with type 1 inflammation) was reduced, along with a marked reduction in *Il17a* expression by γδ T cells.

Mapping the unique subtypes of secretory epithelial cells in the mouse nasal mucosa

Epithelial cell composition in the nose is adapted to the unique position of the nasal mucosa as the initial site of contact with inhaled air, particulate matter, and odorants. Our single-cell analysis of these epithelial subtypes revealed their anatomical distribution across respiratory and olfactory mucosa (**Fig. 5A**, **S7A**, **S7C** and **Table S9**), and transcriptional profile (**Fig. 5B**).

Our location specific analysis of epithelial subsets identified several subsets of epithelial cells dominantly derived from the olfactory mucosa. In addition to the ionocytes and tuft-MVCs we characterized earlier; we found several other specialized epithelial subsets with predominantly olfactory distribution. These included sustentacular cells, two types of mucosal ductal cells and GBCs (**Fig. 5A**). Non-neuronal cells of the olfactory epithelium are classically identified by their expression of *Cyp2g1 (71)* and cytokeratin 18 *Krt18 (72)*. Multiple mouse models use *Cyp2g1* to specifically target the olfactory epithelium without an effect on OSNs (73, 74). Here, we identify two major subsets of *Cyp2g1* expressing cells with unique characteristics: in addition to the supporting sustentacular cells marked by *Muc2*, a distinct second population of epithelial cells was positive for *Cyp2g1,* negative for *Muc2* and instead highly expressed markers of Bowman's gland ductal cells including *Aqp4* and *Aqp5 (75)* (**Fig. 5B, Fig. S7B**). We confirmed Muc2 was ubiquitously and highly expressed marker of sustentacular cells (**Fig. 5C**, **D**). Muc2 expression was limited to the olfactory epithelial sustentacular cells and did not mark ductal cells in the olfactory mucosa (**Fig. 5C-E**). Thus, Muc2 is a specific and sensitive transcriptional and protein marker of sustentacular cells. Notably, sustentacular cells were the main site of *Il33* expression in the nasal mucosa consistent with previous findings (3) (**Fig. 5B**). Co-localization of Aquaporin 5 and DCKL1 defined the second subset of *Cyp2g1*$^+$ olfactory epithelial cells as the cells lining the transepithelial ducts of the Bowman's glands (**Fig. 5F**, **G**).

Notably, this specific subset of Aquaporin 5$^+$ DCLK1$^+$ cells was restricted to the olfactory neuroepithelium and hence we refer to them as transepithelial ductal cells (**Fig. 5G**, **Fig. S7C**). The transepithelial ductal cells are enriched for expression of the PGD_2 receptor DP2 (*Ptgdr*) (**Fig. 5B**), a receptor associated with mucus secretion in humans (66). In addition to the *Aqp5*$^+$/*Dclk1*$^+$ transepithelial ductal cells, we identified a separate population of epithelial cells marked by very high expression of *Aqp5* which were negative for *Dclk1* and *Cyp2g1*. Immunofluorescent histology localized these cells to the submucosal portion of the Bowman's gland ducts (**Fig. 5G**). Although rare, these submucosal ductal cells were quite distinct in their expression of several members of the bactericidal/permeability-increasing protein (BPI) fold family members – *Bpifb3, Bpifb4* and *Bpifb6* (**Fig. 5B**, **Table S6**). These genes initially named and defined for their sequence homology to the gene encoding *Bpifa1* (the BPI long palate and nasal epithelial clone antimicrobial protein Splunc1), have now been shown to encode proteins associated with endoplasmic reticulum and Golgi vesicle trafficking, and their function has been associated with viral replication (76-78). This is notable as we find that the submucosal ductal cells are among the highest expressing subtype for the SARS-CoV2 entry molecule ACE2 (**Fig. S7D-F**).

While Muc2 is restricted to the olfactory mucosa, we find two other subsets of secretory cells with broader distribution in the nasal mucosa: *Muc5b*$^+$/*Tff2*$^+$ mucous cells and GP2$^+$ goblet cells. Our scRNA-seq analysis indicated that GP2$^+$ goblet cells were more numerous in the olfactory portion while the glandular mucous cells were equally distributed in the olfactory and respiratory mucosa (**Fig. 5A**). Nasal goblet cells are marked by the expression of *Gp2* and genes encoding proteins with antimicrobial activity: *Lyz2* for lyzosyme C (79), and *Reg3g*, which encodes regenerating islet-derived protein 3-gamma, a bactericidal C-type lectin with activity against Gram$^+$ bacteria (80) (**Fig. 5B**). Spatial analysis by immunofluorescence demonstrated that GP2 is widely expressed in luminal epithelial cells in the respiratory epithelium (**Fig. 5C**, **E**) and lateral nasal gland (**Fig. S7G**, **H**). The goblet cells of the lateral nasal gland, which is located in the posterior portion of the nose, account for all of the GP2 expression in the olfactory nasal portion (**Fig. 5C** and **Fig. S7G**).

The *Muc5b*$^+$ glandular mucous cells express the highest levels of several transcripts of molecules needed for epithelial defense in addition to their signature expression of *Muc5b*: the trefoil factor *Tff2,* secreted in concert with mucins and involved in epithelial restitution (23) as well as *Bpifa1* encoding the protein Splunc1 important for nasal epithelial defense (81-83) (**Fig. 5B**). We used Muc5b protein as a marker of the glandular mucous cells and found it was highly expressed in 1) the acinar cells of the submucosal Bowman's glands of the olfactory epithelium (**Fig. 5H, I**); 2) the submucosal glands of the respiratory mucosa (**Fig. 5H, J**) and 3) the acinar cells of the lateral nasal glands (**Fig. 5H**). We detected low expression of Muc5b in GP2-expressing goblet cells lining the luminal surface of the respiratory epithelium and lateral nasal gland (**Fig. S7H**, **I**). Consistent with this wide distribution of mucin expressing cells in the nose, we find multiple Periodic Acid Schiff positive cells in the epithelial lining of the respiratory mucosa, septal and lateral nasal glands in addition to submucosal glands in the respiratory mucosa and in the Bowman's glands of the olfactory mucosa (**Fig. S7J**).

Finally, we identified a unique population of epithelial cells marked by very high and specific expression of odorant binding protein (OBP)-encoding genes: *Obp1a, Obp1b, Obp2a* and other members of the lipocalin family: *Lcn11* and *Mup4* (**Fig. 5B**, **Fig. S7L, Table S6**). OBPs are a sub-class of lipocalins, defined by their property of reversibly binding volatile chemicals (odorants) for delivery to the olfactory receptor neurons (84, 85). Because of their

high and unique expression of OBPs, we refer to these cells as OBP expressing (OBPE). Using *in situ* hybridization to localize OBPEs in the nose, we found clusters of cells with very high *Obp1a* mRNA expression consistent with the high and specific *Obp1a* expression in the scRNAseq data (**Fig. S7K, L**). The *Obp1a* clusters were localized in the submucosal area of the lateral nasal gland similar to previous reports of expression of *Obp1a* in rats (86) (**Fig. S7K**). In addition, we found high *Obp1a* expression in the septal submucosal glands (**Fig. 5K, L**). Thus, we identified several sites that might contribute to the transport of odorants to OSNs.

After characterizing the homeostatic epithelial composition of the nose, we analyzed the differential responses of the olfactory and respiratory mucosa to aeroallergen exposure. While mucous cell metaplasia is a classical effect of lung inflammation, the differential dynamics of subsets of secretory cells in the nasal mucosa is unknown. We identified a 1.4- [CI-95: 0.6, 3.3] and 3.9-fold [CI-95: 1.5, 11.1] increase in glandular mucous cells in the epithelium after 1 and 2 *Alternaria* doses respectively (**Fig. 5M** and **Table S9**). We also found a 2.9-fold [1.1, 8.1] increase in GP2$^+$ goblet cells after 2 *Alternaria* doses (**Fig. 5M**). We validated this increase in goblet cells using histology (**Fig. S8A, B**). Differential expression analysis (**Fig. 5N, O** and **Fig. S8C, D**) distinguished between cell-type specific and cell type-independent effects (**Methods**), which identified *Muc5b*$^+$ glandular mucous and *Gp2*$^+$ goblet cells as the most strongly affected cell-types (**Fig. S8C**). Finally, we identified chitinase-like protein 4 (*Chil4*) as the gene most strongly up-regulated after allergen challenge across multiple cell types (**Fig. 5N**, **O**). *Chil4* expression, previously shown to increase in lung type 2 inflammation (87), was upregulated across many cell types after *Alternaria* treatment. However, the greatest increases by far were in *Gp2*$^+$ goblet and *Muc5b*$^+$ mucous cells (**Fig. 5O**).

Induction of stem cell proliferation by allergen inhalation

To determine if dynamic changes in the stem cell compartment in the nose might be responsible for the allergen-induced remodeling, we next focused on the plasticity of olfactory and respiratory epithelial progenitors. Keratin-5 (*Krt5*)-expressing HBCs are a quiescent population of stem cells which become activated after chemical injury and proliferate in order to replenish both the neurons and epithelial cells of the olfactory epithelium (2, 88). HBCs give rise to GBCs, a population of Kit$^+$/Ascl1$^+$ proliferating neurogenic progenitors unique to the olfactory epithelium (3). Consistently, our analysis identified two subsets of basal epithelial cells corresponding to HBCs and GBCs (**Fig. 1A**, **1D**, and **S7A**). While HBCs are also found in the respiratory epithelium, GBCs were enriched in the olfactory epithelium (**Fig. 5A**) as expected.

Aeroallergens such as *Alternaria* activate epithelial cells in the respiratory mucosa leading to direct and indirect (immune cell-mediated) epithelial remodeling (26, 28, 59, 60, 89). Aeroallergen-triggered alterations in the olfactory mucosa and olfactory stem cell responses have not been extensively studied. To identify activated cell populations, we examined the proportion of cycling cells of each type before and after *Alternaria* inhalation, finding that proliferation is strongly and specifically induced in HBCs (**Fig. 6A, 6B** and **Fig. S9A**). This effect was much stronger in the olfactory epithelium which showed a 6.1-fold increase (p=1.4×10^{-8}, Wald test) in the fraction of *Krt5*$^+$ cells which are positive for a cell-cycle gene signature (**Methods**) than in the respiratory (1.8-fold increase, p=2.7×10^{-6}, Wald test) (**Fig. 6B**). The proportion of proliferating GBCs, which represent the highest proportion of proliferating cells in the naïve olfactory mucosa (**Fig. S9A)**, did not change after *Alternaria* (**Fig. S9A, S9B**).

Pseudotime analysis of olfactory neurogenesis identifies a Stmn1⁺ allergen-induced precursor
We isolated the 17,318 CD45⁻ epithelial and neuronal cells from the olfactory epithelium and performed 'pseudo time' analysis (**Fig. 6C** and **Fig. S9C**) using the partition-based graph abstraction (PAGA) algorithm (90). The inferred trajectory of cellular states (**Fig. 6C**) largely recapitulated the topology previously defined by Fletcher *et al*. at homeostasis (3), showing that HBCs give rise to GBCs, which in turn differentiate along a major pathway to OSNs, and a minor pathway to MVCs, which we show here to be tuft cells and ionocytes (**Fig. 1**).

We identified the genes (**Fig. 6D, Fig. S9D, E** and **Table S10**) where expression significantly varied (FDR<0.001, Wald test) along with progression through neurogenesis using generalized additive regression models (**Methods**). Early genes included canonical markers of HBCs, such as *Krt5*, and the transcription factor *Trp63 (*91*)*, while genes at the latest stages included olfactory marker protein (*Omp*), and other markers of mature OSNs, such as *Chga* encoding chromogranin A*, S100a5* and *Olfm1* for olfactomedin 1 (**Fig. S9E**). As expected, GBC markers *Ascl1* and *Kit* were transiently activated during the intermediate stages of neurogenesis (**Fig. 6D**). However, prior to their activation, we observed up-regulation of a module of genes involved in regulation of cell cytoskeleton, including stathmin-1 (*Stmn1*), alpha (*Tuba1a*, *Tuba1b*) and beta-tubulin (*Tubb5*). We validated that stathmin-1 marks a subset of early precursors of OSNs distinct from Krt5⁺ HBCs using immunofluorescent staining (**Fig. 6E**).

We confirmed an increase in proliferating HBCs marked by Keratin-5 and Ki67 after *Alternaria* challenge in the olfactory mucosa by immunofluorescence (**Fig. 6F**). The majority of Ki67⁺ cells were located at the basement membrane consistent with the localization of HBCs. Very few proliferating cells were positive for Tubb3 (Tuj1), a marker of mature and immature neurons (**Fig. S9F and S10D**), but a high proportion were positive for Stathmin1 (**Fig. 6F**, **Fig. S9F**) indicating commitment of this activated population to the neuronal lineage. To quantitate and define the HBC proliferative response to *Alternaria*, we assessed the co-expression of Keratin 5 and Ki67 in the whole nasal mucosa over a time course of 63 hours after *Alternaria* inhalation by FACS (**Fig. S10A**). Proliferating Keratin 5⁺/Ki67⁺ HBCs significantly increase 39 hours after *Alternaria* (a time point that corresponds to our scRNAseq) and that response persisted through later time points up to 63 hours (day 3) (**Fig. 6G, H**). Our morphological assessment of *Alternaria*-induced olfactory responses suggested that the nuclei of a proportion of Keratin 5⁺/Ki67⁺ cells in the olfactory mucosa is larger consistent with a proliferative state (**Fig. 5F**). We tested this using FACS FSC/SSC measures and detected a specific change of morphology in the Keratin 5⁺/Ki67⁺ cells after *Alternaria* inhalation (**Fig. S10B)**. In contrast to the induction of HBC proliferation, we found no change in the proportion of Kit⁺Ki67⁺ GBCs assessed in parallel by FACS (**Fig. S10C**). Despite the significant induction of HBC proliferation, the overall architecture of the nasal mucosa was unperturbed by *Alternaria* inhalation (**Fig. S10D, E**) and the proportion of OMP⁺ OSNs defined by scRNAseq did not significantly change (**Table S9**). Collectively, several lines of evidence suggested that the HBC proliferation induced by *Alternaria* occurs in the absence of profound OSN damage. Confirming that, we found no induction of necrosis or apoptosis pathways by *Alternaria* in OSNs (**Fig. S10F**). Thus, we demonstrated that inhalation of the aeroallergen *Alternaria* induced proliferation of the quiescent HBCs and olfactory neurogenesis in the 36-72 hours after exposure. To our knowledge, this is the first evidence of induction of olfactory neurogenesis in the absence of OSN damage in mice.

Allergen-induced olfactory remodeling is mediated by CysLTs derived from tuft cells

Since the mechanism by which aeroallergens trigger proliferation of olfactory HBCs is not known, and our previous studies had suggested that CysLTs might play a role in epithelial proliferation in the trachea (26), we hypothesized that these lipid mediators might regulate this basal cell regenerative response. Consistent with this possibility, we found that along with its known expression in immune cells, *Cysltr1*, encoding the cognate receptor for LTD_4, is surprisingly enriched in both olfactory stem cell subsets: GBCs and HBCs (**Fig. S11A**).

To determine if CysLTs derived from tuft cells are contributing to olfactory neurogenesis, we analyzed the nasal mucosa of mice with tuft cell-specific deletion of *Ltc4s*, the terminal CysLT biosynthetic enzyme (*Chat*^{Cre}*Ltc4s*$^{fl/fl}$) (28). Our scRNAseq analysis had demonstrated that OSNs in different stages of development and basal cells express intermediate to low levels of EpCAM. Therefore, we sorted EpCAM^{intermediate} cells from mice with tuft cell specific *Ltc4s* deletion (*Chat*^{Cre}*Ltc4s*$^{fl/fl}$) and their controls (*Ltc4s*$^{fl/fl}$) (**Fig. S11B**). Deconvolution analysis (**Methods**) of bulk RNA-seq of these sorted populations revealed that the majority of EpCAM^{intermediate} cells were mature olfactory neurons (OSN) and immature olfactory neurons (ISN) while HBCs and GBCs represented a smaller but noticeable proportion of EpCAM^{intermediate} cells in the naïve state (**Fig. S11C**). Intriguingly, we found a notable dysregulation of the proportions of OSNs, ISNs and basal cells (HBCs and GBCs) in mice with tuft cell-specific *Ltc4s* deletion suggesting a role of tuft cell-derived CysLTs in olfactory neurogenesis (**Fig. S11C, D**). To determine how tuft cell derived CysLTs might regulate olfactory HBC proliferation, we assessed the olfactory mucosa for Ki67^{+} HBCs. Morphologically, in cross-sections, we found no clear difference in olfactory structure or number of proliferating Ki67^{+} cells in the naive state between WT and *Chat*^{Cre}*Ltc4s*$^{fl/fl}$ mice. However, the increase in *Alternaria*-induced proliferation of HBCs was blunted in *Chat*^{Cre}*Ltc4s*$^{fl/fl}$ mice (**Fig. 6I-K**). We then used FACS to evaluate the nasal mucosa for compositional changes using NCAM as a marker of OSNs (EpCAM$^{-/low}$NCAM^{+}) and ISNs (EpCAM^{intermediate} NCAM^{+}) in both *Chat*^{Cre}*Ltc4s*$^{fl/fl}$ mice and in tuft cell deficient *Pou2f3*$^{-/-}$ mice (**Fig. S11E, F**). We confirmed the lack of an effect of deletion of tuft cells or tuft cell derived CysLTs on the olfactory neuronal composition in naïve mice (**Fig. S11E, G**). Furthermore, there was no evidence of an acute change in OSNs or ISNs after *Alternaria* inhalation in WT or deficient mice (**Fig. S11E, G**). In contrast, there was a significant increase in the population of EpCAM^{intermediate}NCAM^{-} cells consisting of basal cells and epithelial cells (**Fig. 6L**), consistent with expansion of the HBC stem cell pool. This expansion was again reduced in *Chat*^{Cre}*Ltc4s*$^{fl/fl}$ mice as well as in *Pou2f3*$^{-/-}$ mice that lack tuft cells.

Discussion:

Across mucosal compartments, tuft cells share a core transcriptional profile defined by components of calcium signaling pathways and effector mediators generated in response to calcium flux. They are thus able to respond to environmental signals with de novo generation of mediators, prominently acetylcholine and eicosanoids. The function of olfactory tuft cells (previously called TRPM5$^+$ MVCs) has proven enigmatic; their genetic ablation leads to aberrant neurotrophin expression (92) and impaired olfactory-guided behaviors, albeit only after extended exposure to strong odorants (12). Tuft cell activation through chemical (strong odorants or bacterial lysate) or thermal (cold temperatures) stimulation leads to acetylcholine-mediated calcium flux in olfactory sustentacular cells and modulates the responses to xenobiotic substances in the olfactory mucosa (11, 13). Our findings provide the first evidence of the role of tuft cells as regulators of the neuroepithelial stem cell pool downstream of allergen sensing.

The olfactory neuroepithelium is unique among neuronal tissues in its regenerative capacity (93). The OSNs have a relatively short life span and continuously regenerate from proliferating GBCs, in turn derived from normally quiescent HBCs, which can be activated after necrosis induced by chemical injury (2, 88). Prior to our study, chronic inflammation induced by olfactory-specific TNF overexpression was the only established mouse model of HBC activation that leads to olfactory neuro-regeneration and remodeling in the absence of necrosis (73, 74). Notably, this model is also associated with HBC upregulation of the IL-13 receptor (*Il13ra1*), suggesting that inflammation in the olfactory epithelium primes olfactory stem cells to respond to type 2 cytokines, regardless of the polarization of the immune response (type 1 or type 2). Here we show that a single aeroallergen inhalation induces robust stem cell proliferation in the absence of necrosis or apoptosis of OSNs, defining a new model of physiologic HBC activation.

We used single-cell transcriptomics to map the enzymes needed to generate eicosanoids and their cognate receptors, enabling us to identify targets of tuft cell-derived CysLTs and define a more complete picture of the intercellular signaling network within the nasal mucosa. In the intestine, tuft cells are known to activate local ILCs via both CysLTs and the cytokine IL-25, leading to stem cell regulation via ILC-derived mediators, particularly IL-13 (17, 24, 25). We surprisingly found that both the HBC and GBC reservoirs of neuroepithelial stem cells express the eicosanoid receptor *Cysltr1*, raising the possibility of direct regulation of the stem cell compartment. Our results are consistent with Lemons et al. (14), who identify basal stem cell proliferation in response to prolonged chemical injury, which is abolished in Skn-1a (Pou2f3)-knockout mice, a model of nasal tuft cell (TRPM5$^+$ MVC) ablation. Given the lack of a cellular process extending to the basal layer, Lemons et al. speculated that TRPM5$^+$ MVCs did not regulate HBC proliferation directly. We identify the missing molecular message by which nasal tuft cells induce proliferation in the HBC compartment, but future study is required to conclusively identify the target populations and whether ILCs or other immune cells act as intermediate links in the circuit.

Both scRNAseq and immunolocalization demonstrated a previously unappreciated diversity of epithelial cells in the olfactory mucosa, particularly, a surprisingly rich reservoir of tuft cells and ionocytes in the nasal respiratory and olfactory mucosa, two sensory epithelial types recently characterized as sparse, isolated cells in diverse epithelial tissues. We find that this composition of the MVC compartment is conserved in human nasal mucosa, also composed of tuft cells and ionocytes, human cell types which share remarkable molecular similarity with their murine counterparts, including expression of eicosanoid enzymes *Alox5*, *Alox5ap* and *Ltc4s*. However, whether they possess the same capacity to generate eicosanoids to regulate the

olfactory stem cell compartment is not yet known. Intriguingly, inhibiting CysLT generation using the 5-lipoxygenase inhibitor zileuton improves olfactory function among other parameters of nasal inflammation in patients with aspirin-exacerbated respiratory disease, a CRS phenotype associated with high levels of CysLT production (94, 95).

In sum, we provide extensive characterization of the rare subsets of nasal epithelial cells, conclusively identifying MVCs as recently described tuft cells and ionocytes and defining new molecularly and morphologically distinct subsets. We provide genetic evidence that lipid mediators generated by tuft cells play a surprising role in regulating the stem cell compartment which supplies the regenerative capacity for the olfactory neuroepithelium after allergen inhalation. Together, these data deepen our understanding of the extensive epithelial heterogeneity in the nose and demonstrate that the functional capacity of tuft cells extends beyond triggering inflammation as they are also potent regulators of tissue homeostasis and transformation.

References:

1. C. Bachert *et al.*, in *Mucosal Immunology, Fourth Edition*. (2016), chap. 100, pp. 1899-1921.
2. C. T. Leung, P. A. Coulombe, R. R. Reed, Contribution of olfactory neural stem cells to tissue maintenance and regeneration. *Nat Neurosci* **10**, 720-726 (2007).
3. R. B. Fletcher *et al.*, Deconstructing Olfactory Stem Cell Trajectories at Single-Cell Resolution. *Cell Stem Cell* **20**, 817-830.e818 (2017).
4. C. L. Beites, S. Kawauchi, C. E. Crocker, A. L. Calof, Identification and molecular regulation of neural stem cells in the olfactory epithelium. *Exp Cell Res* **306**, 309-316 (2005).
5. Y. Suzuki, M. Takeda, A. I. Farbman, Supporting cells as phagocytes in the olfactory epithelium after bulbectomy. *J Comp Neurol* **376**, 509-517 (1996).
6. A. Hansen, T. E. Finger, Is TrpM5 a reliable marker for chemosensory cells? Multiple types of microvillous cells in the main olfactory epithelium of mice. *BMC Neurosci* **9**, 115 (2008).
7. W. Lin, E. A. Ezekwe, Jr., Z. Zhao, E. R. Liman, D. Restrepo, TRPM5-expressing microvillous cells in the main olfactory epithelium. *BMC Neurosci* **9**, 114 (2008).
8. P. L. Weng, M. Vinjamuri, C. E. Ovitt, Ascl3 transcription factor marks a distinct progenitor lineage for non-neuronal support cells in the olfactory epithelium. *Sci Rep* **6**, 38199 (2016).
9. C. Jia *et al.*, An IP3R3- and NPY-expressing microvillous cell mediates tissue homeostasis and regeneration in the mouse olfactory epithelium. *PLoS One* **8**, e58668 (2013).
10. W. Lin, T. Ogura, R. F. Margolskee, T. E. Finger, D. Restrepo, TRPM5-Expressing Solitary Chemosensory Cells Respond to Odorous Irritants. *J Neurophysiol* **99**, 1451-1460 (2008).
11. T. Ogura *et al.*, Cholinergic microvillous cells in the mouse main olfactory epithelium and effect of acetylcholine on olfactory sensory neurons and supporting cells. *J Neurophysiol* **106**, 1274-1287 (2011).
12. K. Lemons *et al.*, Lack of TRPM5-Expressing Microvillous Cells in Mouse Main Olfactory Epithelium Leads to Impaired Odor-Evoked Responses and Olfactory-Guided Behavior in a Challenging Chemical Environment. *eNeuro* **4**, (2017).
13. Z. Fu, T. Ogura, W. Luo, W. Lin, ATP and Odor Mixture Activate TRPM5-Expressing Microvillous Cells and Potentially Induce Acetylcholine Release to Enhance Supporting Cell Endocytosis in Mouse Main Olfactory Epithelium. *Front Cell Neurosci* **12**, 10167-10116 (2018).
14. K. Lemons, Z. Fu, T. Ogura, W. Lin, TRPM5-expressing Microvillous Cells Regulate Region-specific Cell Proliferation and Apoptosis During Chemical Exposure. *Neurosci* **434**, 171-190 (2020).
15. S. Kaske *et al.*, TRPM5, a taste-signaling transient receptor potential ion-channel, is a ubiquitous signaling component in chemosensory cells. *BMC Neurosci* **8**, 49 (2007).
16. M. Tizzano, M. Cristofoletti, A. Sbarbati, T. E. Finger, Expression of Taste Receptors in Solitary Chemosensory Cells of Rodent Airways. *BMC Pulm Med* **11**, (2011).
17. M. R. Howitt *et al.*, Tuft cells, taste-chemosensory cells, orchestrate parasite type 2 immunity in the gut. *Science*, 1-9 (2016).
18. B. D. Gulbransen, T. R. Clapp, T. E. Finger, S. C. Kinnamon, Nasal Solitary Chemoreceptor Cell Responses to Bitter and Trigeminal Stimulants In Vitro. *J Neurophysiol* **99**, 2929-2937 (2008).
19. G. Krasteva *et al.*, Cholinergic chemosensory cells in the trachea regulate breathing. *Proc Natl Acad Sci USA* **108**, 9478-9483 (2011).
20. C. Bezencon *et al.*, Murine intestinal cells expressing Trpm5 are mostly brush cells and express markers of neuronal and inflammatory cells. *J Comp Neurol* **509**, 514-525 (2008).
21. G. Krasteva, B. J. Canning, T. Papadakis, W. Kummer, Cholinergic brush cells in the trachea mediate respiratory responses to quorum sensing molecules. *Life Sci* **91**, 992-996 (2012).
22. D. T. Montoro *et al.*, A Revised Airway Epithelial Hierarchy Includes CFTR-expressing Ionocytes. *Nature* **560**, 319-324 (2018).
23. A. L. Haber *et al.*, A single-cell survey of the small intestinal epithelium. *Nature* **551**, 333-339 (2017).

24. J. von Moltke, M. Ji, H.-E. Liang, R. M. Locksley, Tuft-cell-derived IL-25 regulates an intestinal ILC2–epithelial response circuit. *Nature* **529**, 221-225 (2016).
25. F. Gerbe *et al.*, Intestinal epithelial tuft cells initiate type 2 mucosal immunity to helminth parasites. *Nature* **529**, 226-230 (2016).
26. L. G. Bankova *et al.*, The Cysteinyl Leukotriene 3 Receptor Regulates Expansion of IL-25-producing Airway Brush Cells Leading to Type 2 Inflammation. *Sci Immunol* **3**, eaat9453 (2018).
27. S. Ualiyeva *et al.*, Airway Brush Cells Generate Cysteinyl Leukotrienes Through the ATP Sensor P2Y2. *Sci Immunol* **5**, eaax7224 (2020).
28. S. Ualiyeva *et al.*, Tuft cell-produced cysteinyl leukotrienes and IL-25 synergistically initiate lung type 2 inflammation. *Sci Immunol* **6**, eabj0474 (2021).
29. T. Yamaguchi *et al.*, Skn-1a/Pou2f3 is required for the generation of Trpm5-expressing microvillous cells in the mouse main olfactory epithelium. *BMC Neurosci* **15**, 13 (2014).
30. M. Ohmoto, I. Matsumoto, A. Yasuoka, Y. Yoshihara, K. Abe, Genetic tracing of the gustatory and trigeminal neural pathways originating from T1R3-expressing taste receptor cells and solitary chemoreceptor cells. *Mol Cell Neurosci* **38**, 505-517 (2008).
31. M. Ohmoto, N. Maeda, K. Abe, Y. Yoshihara, I. Matsumoto, Genetic tracing of the neural pathway for bitter taste in t2r5-WGA transgenic mice. *Biochem Biophys Res Commun* **400**, 734-738 (2010).
32. M. Ohmoto *et al.*, Pou2f3/Skn-1a is necessary for the generation or differentiation of solitary chemosensory cells in the anterior nasal cavity. *Biosci Biotechnol Biochem* **77**, 2154-2156 (2013).
33. J. Yamashita, M. Ohmoto, T. Yamaguchi, I. Matsumoto, J. Hirota, Skn-1a/Pou2f3 functions as a master regulator to generate Trpm5-expressing chemosensory cells in mice. *PLoS One* **12**, e0189340 (2017).
34. S. Pfister *et al.*, Novel role of cystic fibrosis transmembrane conductance regulator in maintaining adult mouse olfactory neuronal homeostasis. *J Comp Neurol* **523**, 406-430 (2015).
35. A. Ablimit *et al.*, Immunolocalization of water channel aquaporins in the vomeronasal organ of the rat: expression of AQP4 in neuronal sensory cells. *Chem Senses* **33**, 481-488 (2008).
36. M. Tizzano, T. E. Finger, Chemosensors in the nose: guardians of the airways. *Physiology (Bethesda)* **28**, 51-60 (2013).
37. M. S. Nadjsombati *et al.*, Detection of Succinate by Intestinal Tuft Cells Triggers a Type 2 Innate Immune Circuit. *Immunity* **49**, 33-41 e37 (2018).
38. A. M. Newman *et al.*, Determining cell type abundance and expression from bulk tissues with digital cytometry. *Nat Biotechnol* **37**, 773-782 (2019).
39. D. D. Gerendasy, J. G. Sutcliffe, RC3/neurogranin, a postsynaptic calpacitin for setting the response threshold to calcium influxes. *Mol Neurobiol* **15**, 131-163 (1997).
40. T. E. Finger *et al.*, Solitary Chemoreceptor Cells in the Nasal Cavity Serve as Sentinels of Respiration. *Proc Natl Acad Sci USA* **100**, 8981-8986 (2003).
41. B. D. Gulbransen, T. E. Finger, Solitary chemoreceptor cell proliferation in adult nasal epithelium. *J Neurocytol* **34**, 117-122 (2005).
42. R. J. Lee *et al.*, Bitter and sweet taste receptors regulate human upper respiratory innate immunity. *J Clin Invest* **124**, 1393-1405 (2014).
43. R. J. Lee *et al.*, T2R38 taste receptor polymorphisms underlie susceptibility to upper respiratory infection. *J Clin Invest* **122**, 4145-4159 (2012).
44. J. von Moltke, M. Ji, H. E. Liang, R. M. Locksley, Tuft-cell-derived IL-25 regulates an intestinal ILC2-epithelial response circuit. *Nature* **529**, 221-225 (2016).
45. J. D. Barros-Silva *et al.*, Single-Cell Analysis Identifies LY6D as a Marker Linking Castration-Resistant Prostate Luminal Cells to Prostate Progenitors and Cancer. *Cell Rep* **25**, 3504-3518 e3506 (2018).
46. G. Upadhyay, Emerging Role of Lymphocyte Antigen-6 Family of Genes in Cancer and Immune Cells. *Front Immunol* **10**, 819 (2019).

47. A. Mayama *et al.*, OLFM4, LY6D and S100A7 as potent markers for distant metastasis in estrogen receptor-positive breast carcinoma. *Cancer Sci* **109**, 3350-3359 (2018).
48. F. Gerbe, B. Brulin, L. Makrini, C. Legraverend, P. Jay, DCAMKL-1 expression identifies Tuft cells rather than stem cells in the adult mouse intestinal epithelium. *Gastroenterology* **137**, 2179-2180; author reply 2180-2171 (2009).
49. R. A. Hall, Autonomic modulation of olfactory signaling. *Science Signaling* **4**, pe1 (2011).
50. R. J. Lee, N. A. Cohen, Sinonasal solitary chemosensory cells "taste" the upper respiratory environment to regulate innate immunity. *Am J Rhinol Allergy* **28**, 366-373 (2014).
51. M. A. Kohanski *et al.*, Solitary chemosensory cells are a primary epithelial source of IL-25 in patients with chronic rhinosinusitis with nasal polyps. *J Allergy Clin Immunol* **142**, 460-469 e467 (2018).
52. N. N. Patel *et al.*, Fungal extracts stimulate solitary chemosensory cell expansion in noninvasive fungal rhinosinusitis. *Int Forum Allergy Rhinol* **9**, 730-737 (2019).
53. J. Ordovas-Montanes *et al.*, Allergic Inflammatory Memory in Human Respiratory Epithelial Progenitor Cells. *Nature* **560**, 649-654 (2018).
54. D. T. Moran, J. C. Rowley, 3rd, B. W. Jafek, Electron microscopy of human olfactory epithelium reveals a new cell type: the microvillar cell. *Brain Res* **253**, 39-46 (1982).
55. E. E. Morrison, R. M. Costanzo, Morphology of the human olfactory epithelium. *J Comp Neurol* **297**, 1-13 (1990).
56. M. A. Durante *et al.*, Single-cell Analysis of Olfactory Neurogenesis and Differentiation in Adult Humans. *Nat Neurosci* **23**, 323-326 (2020).
57. C. Schneider, C. E. O'Leary, R. M. Locksley, Regulation of immune responses by tuft cells. *Nat Rev Immunol*, 1-10 (2019).
58. T. Kobayashi *et al.*, Asthma-related environmental fungus, Alternaria, activates dendritic cells and produces potent Th2 adjuvant activity. *J Immunol* **182**, 2502-2510 (2009).
59. H. Kouzaki, K. Iijima, T. Kobayashi, S. M. O'Grady, H. Kita, The danger signal, extracellular ATP, is a sensor for an airborne allergen and triggers IL-33 release and innate Th2-type responses. *J Immunol* **186**, 4375-4387 (2011).
60. T. A. Doherty *et al.*, STAT6 regulates natural helper cell proliferation during lung inflammation initiated by Alternaria. *Am J Physiol Lung Cell Mol Physiol* **303**, L577-588 (2012).
61. J. W. McGinty *et al.*, Tuft-Cell-Derived Leukotrienes Drive Rapid Anti-helminth Immunity in the Small Intestine but Are Dispensable for Anti-protist Immunity. *Immunity* **52**, 528-541.e527 (2020).
62. T. A. Doherty *et al.*, Lung type 2 innate lymphoid cells express cysteinyl leukotriene receptor 1, which regulates TH2 cytokine production. *JACI* **132**, 205--213 (2013).
63. J. von Moltke *et al.*, Leukotrienes provide an NFAT-dependent signal that synergizes with IL-33 to activate ILC2s. *J Exp Med* **214**, 27-37 (2017).
64. N. A. Barrett *et al.*, Dectin-2 mediates Th2 immunity through the generation of cysteinyl leukotrienes. *J Exp Med* **208**, 593-604 (2011).
65. N. A. Barrett *et al.*, Cysteinyl leukotriene 2 receptor on dendritic cells negatively regulates ligand-dependent allergic pulmonary inflammation. *J Immunol* **189**, 4556-4565 (2012).
66. T. Oguma, K. Asano, A. a. Ishizaka, Role of prostaglandin D2 and its receptors in the pathophysiology of asthma. *Allergol Int* **57**, 307-312 (2008).
67. L. G. Bankova *et al.*, Leukotriene E4 Elicits Respiratory Epithelial Cell Mucin Release Through the G-protein-coupled Receptor, GPR99. *Proc Natl Acad Sci USA* **113**, 6242-6247 (2016).
68. C. S. Smillie *et al.*, Intra- and Inter-cellular Rewiring of the Human Colon during Ulcerative Colitis. *Cell* **178**, 714-730.e722 (2019).
69. R. Vento-Tormo *et al.*, Single-cell Reconstruction of the Early Maternal–fetal Interface in Humans. *Nature* **563**, 347-353 (2018).
70. J. A. Ramilowski *et al.*, A draft network of ligand-receptor-mediated multicellular signalling in human. *Nat Commun* **6**, 7866 (2015).

71. T. T. Yu *et al.*, Differentially expressed transcripts from phenotypically identified olfactory sensory neurons. *J Comp Neurol* **483**, 251-262 (2005).
72. J. E. Schwob, S. L. Youngentob, R. C. Mezza, Reconstitution of the rat olfactory epithelium after methyl bromide-induced lesion. *J Comp Neurol* **359**, 15-37 (1995).
73. M. Chen, R. R. Reed, A. P. Lane, Acute inflammation regulates neuroregeneration through the NF-kappaB pathway in olfactory epithelium. *Proc Natl Acad Sci USA* **114**, 8089-8094 (2017).
74. M. Chen, R. R. Reed, A. P. Lane, Chronic Inflammation Directs an Olfactory Stem Cell Functional Switch from Neuroregeneration to Immune Defense. *Cell Stem Cell* **25**, 501-513 e505 (2019).
75. T. T. Solbu, T. Holen, Aquaporin pathways and mucin secretion of Bowman's glands might protect the olfactory mucosa. *Chem Senses* **37**, 35-46 (2012).
76. A. S. Evans, N. J. Lennemann, C. B. Coyne, BPIFB3 interacts with ARFGAP1 and TMED9 to regulate non-canonical autophagy and RNA virus infection. *J Cell Sci* **134**, jcs251835 (2021).
77. A. S. Evans, N. J. Lennemann, C. B. Coyne, BPIFB3 Regulates Endoplasmic Reticulum Morphology To Facilitate Flavivirus Replication. *J Virol* **94**, e00029-00020 (2020).
78. S. Morosky, N. J. Lennemann, C. B. Coyne, BPIFB6 Regulates Secretory Pathway Trafficking and Enterovirus Replication. *J Virol* **90**, 5098-5107 (2016).
79. D. M. Irwin, J. M. Biegel, C. B. Stewart, Evolution of the mammalian lysozyme gene family. *BMC Evol Biol* **11**, 166 (2011).
80. S. Mukherjee *et al.*, Regulation of C-type lectin antimicrobial activity by a flexible N-terminal prosegment. *J Biol Chem* **284**, 4881-4888 (2009).
81. W. M. Weston *et al.*, Differential display identification of plunc, a novel gene expressed in embryonic palate, nasal epithelium, and adult lung. *J Biol Chem* **274**, 13698-13703 (1999).
82. M. Musa *et al.*, Differential localisation of BPIFA1 (SPLUNC1) and BPIFB1 (LPLUNC1) in the nasal and oral cavities of mice. *Cell Tissue Res* **350**, 455-464 (2012).
83. L. Bingle *et al.*, SPLUNC1 (PLUNC) is expressed in glandular tissues of the respiratory tract and in lung tumours with a glandular phenotype. *J Pathol* **205**, 491-497 (2005).
84. J. Pevsner, R. R. Reed, P. G. Feinstein, S. H. Snyder, Molecular cloning of odorant-binding protein: member of a ligand carrier family. *Science* **241**, 336-339 (1988).
85. M. Tegoni *et al.*, Mammalian Odorant Binding Proteins. *Biochimica et Biophysica Acta* **1482**, 229-240 (2000).
86. J. Pevsner, P. M. Hwang, P. B. Sklar, J. C. Venable, S. H. Snyder, Odorant-binding protein and its mRNA are localized to lateral nasal gland implying a carrier function. *Proc Natl Acad Sci USA* **85**, 2383-2387 (1988).
87. T. E. Sutherland *et al.*, Chitinase-like proteins promote IL-17-mediated neutrophilia in a tradeoff between nematode killing and host damage. *Nat Immunol* **15**, 1116-1125 (2014).
88. L. Gadye *et al.*, Injury Activates Transient Olfactory Stem Cell States with Diverse Lineage Capacities. *Cell Stem Cell* **21**, 775-790.e779 (2017).
89. T. A. Doherty *et al.*, Alternaria induces STAT6-dependent acute airway eosinophilia and epithelial FIZZ1 expression that promotes airway fibrosis and epithelial thickness. *J Immunol* **188**, 2622-2629 (2012).
90. F. A. Wolf *et al.*, PAGA: graph abstraction reconciles clustering with trajectory inference through a topology preserving map of single cells. *Genome Biol* **20**, 59 (2019).
91. R. B. Fletcher *et al.*, p63 regulates olfactory stem cell self-renewal and differentiation. *Neuron* **72**, 748-759 (2011).
92. A. AlMatrouk *et al.*, Chemical Exposure-Induced Changes in the Expression of Neurotrophins and Their Receptors in the Main Olfactory System of Mice Lacking TRPM5-Expressing Microvillous Cells. *Int J Mol Sci* **19**, 2939-2921 (2018).
93. E. R. Kandel, J. H. Schwartz, T. M. Jessell, S. A. Siegelbaum, A. J. Hudspeth, *Principles of Neural Science*. (McGraw-Hill, New York, NY, ed. 5th, 2013).

94. T. M. Laidlaw, J. A. Boyce, Aspirin-Exacerbated Respiratory Disease - New Prime Suspects. *N Engl J Med* **374**, 484-488 (2016).
95. B. Dahlen *et al.*, Benefits from adding the 5-lipoxygenase inhibitor zileuton to conventional therapy in aspirin-intolerant asthmatics. *Am J Respir Crit Care Med* **157**, 1187-1194 (1998).
96. S. Ualiyeva, A. A. Boyd, N. A. Barrett, L. G. Bankova, Isolation of Nasal Brush Cells for Single-cell Preparations. *Bio Protoc* **11**, e4163 (2021).
97. G. Finak *et al.*, MAST: a flexible statistical framework for assessing transcriptional changes and characterizing heterogeneity in single-cell RNA sequencing data. *Genome Biol* **16**, 1-13 (2015).
98. E. R. Gansner, Y. Koren, S. North, in *Lecture Notes in Computer Science*. (Springer Berlin Heidelberg, Berlin, Heidelberg, 2005), pp. 239-250.
99. M. S. Kowalczyk *et al.*, Single-cell RNA-seq reveals changes in cell cycle and differentiation programs upon aging of hematopoietic stem cells. *Genome Res* **25**, 1860-1872 (2015).
100. L. Scrucca, M. Fop, T. B. Murphy, A. E. Raftery, mclust 5: Clustering, Classification and Density Estimation Using Gaussian Finite Mixture Models. *R J* **8**, 289-317 (2016).
101. F. A. Wolf, P. Angerer, F. J. Theis, SCANPY: large-scale single-cell gene expression data analysis. *Genome Biol* **19**, 1-5 (2018).
102. V. A. Traag, L. Waltman, N. J. van Eck, From Louvain to Leiden: guaranteeing well-connected communities. *Sci Rep* **9**, 5233 (2019).
103. L. Albergante *et al.*, Robust and Scalable Learning of Complex Intrinsic Dataset Geometry via ElPiGraph. *Entropy* **22**, 296 (2020).
104. S. N. Wood, Fast stable restricted maximum likelihood and marginal likelihood estimation of semiparametric generalized linear models. *J R Stat Soc Series B Stat Methodol* **73**, 3--36 (2011).
105. J. X. Binder *et al.*, COMPARTMENTS: unification and visualization of protein subcellular localization evidence. *Database* **2014**, bau012 (2014).
106. B. Li, C. N. Dewey, RSEM: accurate transcript quantification from RNA-Seq data with or without a reference genome. *BMC Bioinform.* **12**, 323 (2011).
107. P.-C. Bürkner, brms: An R Package for Bayesian Multilevel Models Using Stan. *J Stat Softw* **80**, 1-28 (2017).

Acknowledgments: We thank Adam Chicoine, Gerald Watts, Zhu Zhu and Kevin Wei from the Brigham and Women's Hospital Center for Cellular Profiling for their invaluable assistance with cell isolation and single-cell RNA sequencing. We gratefully acknowledge Leslie Gaffney for help with arranging figures, and Daniel Montoro for technical advice. We are grateful to Charles Vidoudez and Sunia Trauger from the Harvard Center for Mass Spectrometry for their expertise and help setting up the mass spectrometry assays for CysLTs. We are also thankful to Dr. Lisa Goodrich at the Department of Neurobiology at Harvard Medical School for providing reagents and infrastructure for in situ hybridization. *Pou2f3*$^{-/-}$ mice are available from Dr. Matsumoto under a material transfer agreement with the Monell Chemical Senses Center. Schematic diagrams were created using BioRender.

Funding: This work was supported by grants from the National Institutes of Health grant K08 AI132723 (to LGB), 1R21AI154345 (to LGB and ALH), 5T32AI007306 (to JAB, SU), R01AI078908, R37AI052353, R01AI136041, R01HL136209 (to JAB), U19 AI095219 (to NAB, JAB), R01AI134989 (to NAB), AAAAI Foundation Faculty Development Award and Joycelyn C. Austen Fund for Career Development of Women Physician Scientists (to LGB), Parker B. Francis Fellowship (to ALH) and a generous donation by the Vinik family (to LGB).

Author contributions: Conceptualization: ALH, LGB. Methodology: LGB, ALH, EL, SU. Investigation: SU, EL, LGB, ALH, AAB, CW, JL, ECA. Writing: LGB, ALH, JAB, NAB, IM, EL, SU. Funding acquisition: LGB, JAB, NAB, ALH. Resources: TML, KMB, RR, AM, IM and JAB.

Competing interests: Authors declare that they have no competing interests.

Data and materials availability: All data is deposited in GEO (GSEXXXX) and in the Single Cell Portal (https://portals.broadinstitute.org/single_cell). All code required to reproduce the main steps of the analysis will be made available on request.

List of Supplementary Materials:

Materials and Methods

Supplementary Figures:
Figure **S1**: Isolation of single-cell suspensions from nasal respiratory and olfactory epithelium.
Figure **S2**: Anatomical and molecular characterization of olfactory sensory neuron subtypes.
Figure **S3**: Three morphologically distinct types of nasal tuft cells share a common molecular profile.
Figure **S4**: Neurogranin acts as a novel tuft cell marker in multiple subtypes.
Figure **S5**: Single-cell mapping of immune cell subtypes in the naive nasal mucosa.
Figure **S6**: Effects of allergic inflammation on gene expression and cell type proportions in the nasal immune system.
Figure **S7**: Expression of SARS-CoV-2 receptor ACE2 in epithelial cells and marker genes of differentiated mucosal subtypes.
Figure **S8**: Effects of allergic inflammation on gene expression and cell type proportions in the nasal epithelium.
Figure **S9**: Pseudo-time analysis identifies novel marker genes for stages of olfactory neurogenesis.
Figure **S10**: Nasal olfactory mucosa architecture is preserved after *Alternaria* inhalation.
Figure **S11**: Bulk RNA sequencing of Ltc4s-ablated mice confirms role of cysteinyl leukotrienes in olfactory neurogenesis.

Supplementary Tables:
Table **S1**: Known marker gene sets used for interpretation of cell clusters.
Table **S2**. Molecular signatures for all cell types in nasal epithelium.
Table **S3**. Molecular signatures for novel subsets of nasal tuft cells.
Table **S4**. Marker genes for human nasal tuft cells and ionocytes.
Table **S5**. Known gene sets for eicosanoid synthesis.
Table **S6**. Molecular signatures for epithelial and immune cell subsets in the nose.

Table **S7.** Cell type-specific gene expression dynamics after allergic inflammation.
Table **S8**. Modulation of cell-cell signaling during allergic inflammation.
Table **S9**. Cell type composition dynamics during allergic inflammation.
Table **S10**. Gene expression dynamics during olfactory neurogenesis.

Figure Legends:

Fig. 1. Tuft cells and ionocytes comprise two MVC types of the olfactory epithelium. (**A**). tSNE embedding of 13,052 nasal epithelial cells (*n*=4 mice), colored by unsupervised clustering. (**B**) Heatmap shows the fraction of cells (color bar) of each type (rows) of each cell type (columns) using a random forest classifier trained on the tracheal epithelium. (**C**) Fraction (x-axis) of ionocytes in all epithelial cells from each mouse (points), compared to tracheal epithelium. (**D**. Heatmap shows expression (row-wise z-score of $\log_2$(TPM+1). (color bar) of top 50 genes (rows) specific to each cell type (FDR<0.05); two selected genes are shown. (**E**) Cross-section of the nasal olfactory epithelium stained for ChAT-eGFP, cochlin, OMP (top image), ChAT-eGFP and cochlin (lower left image), and ChAT-eGFP and CFTR (lower right image). Hoechst is used to mark nuclei in all images. (**F**) Top 30 pan-tissue tuft cell marker genes (y-axis) ranked by out of bag accuracy (x-axis) from random forest classification. (**G**) Heatmap shows expression (row-wise z-score of log2(TPM+1). (color bar) of top tuft cell marker genes in tuft cells and other epithelial cells across three tissues: nasal, tracheal and gut. (**H-I**) Liquid chromatography-mass spectrometry. Representative chromatograms for LTC_4 and LTE_4 (**H**) and LTC_4 and LTE_4 quantification (**I**) at 30 min after *ex vivo* stimulation of tuft cells with HBSS (control), ATP-γ-S (0.5 mM) or A23187 (1 μM). Data are means ± SEM from 2-3 independent experiments, each dot represents a separate biological replicate. Mann-Whitney tests were used to determine significance in pairwise comparison of responses.

Fig. 2. Single-cell analysis identifies nasal tuft cell heterogeneity. (**A**) tSNE embedding of 5,594 tuft cells derived from ChAT-eGFP mice colored by unsupervised clustering into subsets. (**B**) Heatmaps show the expression level (row-wise z-score of $\log_2$(TPM+1), color bar) of marker (left) and receptor genes (right) specifically expressed (FDR<0.01) by each subset (color bars). Adrenergic and cholinergic receptors are highlighted in bold. (**C**) Heatmap shows the fraction of cells (color bar) of each type (rows) of each cell type (columns) using a random forest classifier trained on previously published scRNA-seq profiling of the tracheal epithelium (22). (**D**) tSNE plots display expression in $\log_2$(TPM) + 1 (color bar) for shared tuft cell markers and subtype markers. (**E-L**) Immunolocalization of tuft cell subsets. (**E**) Cross section through the anterior nasal cavity at the level of the nasal septum captures the olfactory epithelium (top) and respiratory epithelium (bottom). OMP reactivity delineates the OSNs and OSN axons co-stained with neurogranin. Arrows point at neurogranin positive cells. (**F-H**) Tuft-MVC expression of ChAT-eGFP, neurogranin (**F, H**) and advillin (**G**) in the olfactory (**F**, **G**) and respiratory (**H**) mucosa. (**I**) Cross section through the posterior section of the nasal cavity captures the olfactory epithelium (top left), respiratory epithelium (bottom center) and lateral nasal gland (right). OMP reactivity delineates the OSNs co-stained with neurogranin and DCLK1. Inserts show high magnification of the olfactory mucosa (lower left) and the respiratory epithelium lining the lateral nasal gland (top right). (**J**) Expression of ChAT-eGFP and advillin (left) or DCLK1 (right) in tuft cells lining the epithelium of the lateral nasal gland. **K-L**. Tuft-SCC expression of

ChAT-eGFP and advillin (**K**), neurogranin, Gα gustducin (**L**). Hoechst was used for nuclear staining.
(**M-O**) *In situ* hybridization with RNAscope probe for *Ltc4s*. Tuft cells were distinguished based on immunoreactivity for advillin and neurogranin. Representative images of tuft-MVC (**M**), tuft-Gland (**N**) and tuft-SCC (**O**) Nuclear staining with DAPI.

Fig. 3. Single-cell and histological analysis of human nasal mucosa reveals tuft cells and ionocytes. (**A**) tSNE embeddings of 18,987 human nasal epithelial cells (53) showing new re-analysis by unsupervised clustering revealing a group containing tuft cells and ionocytes (inset). (**B**) Heatmap (row-wise z score, color bar) of DE genes (FDR<0.25, rows) among the 68 tuft cells and ionocytes (columns)(53). (**C, D**) Immunofluorescence of respiratory epithelium from ethmoid sinus and superior turbinates of patients with CRS (*n*=2) stained with EpCAM in combination with DCLK1 (**C**) and advillin (**D**). (**E**) tSNE embeddings of 3,528 olfactory epithelial, immune and neuronal cells (56) showing new re-analysis by unsupervised clustering revealing a cluster of MVCs containing tuft cells and ionocytes (inset). (**F**) Heatmap (row-wise z score, color bar) of DE genes (FDR<0.05, rows) among the 116 identified MVCs (56). Selected identified known marker genes are labeled. (**G-I**) Normal superior turbinate tissue collected from a patient undergoing trans-sphenoidal resection of pituitary adenoma was immunostained for NCAM1 and OMP (to mark OSNs) and advillin (**G**) or FOXI1 (**H, I**) to mark tuft cells and ionocytes, respectively. Arrow pointing in **G** at an olfactory axon bundle in the submucosa.

Fig. 4. Single-cell analysis of intercellular communication and compositional shifts during allergic inflammation in the mouse nasal mucosa. (**A**)**.** tSNE embedding of 50,448 cells from nasal mucosa of naïve (left, *n*=4 mice), and treated with 1 dose (center, *n*=3 mice) and two doses of inhaled *Alternaria* (right, *n*=2 mice), cell type lineages identified by unsupervised clustering are shown (color legend). (**B**) Tree map plot shows the cell-type composition (size of rectangles) of the immune compartment in naïve mice. (**C**) Immune cell subset frequency as a percentage of $CD45^+$ cells defined by FACS from naïve and *Alternaria*-challenged mice (x-axis). (**D**) Network visualizations show putative targets of tuft cell-derived eicosanoids in the epithelial (top), lymphoid (middle) and myeloid (bottom) compartments. Any cell type with at least 10% of cells expressing the cognate receptor (labeled text) for a given eicosanoid (color legend) is shown. Arrow thickness shows the fraction of target cells expressing the receptor. (**E**). Density histograms show the posterior distribution from Bayesian Dirichlet Multinomial regression modeling (**Methods**) of log fold-change estimates (x axis) for the effect of one (orange) and two (red) doses of *Alternaria* on the proportion of each immune cell type in the lymphoid (left) and myeloid (right) lineages. Black dot: point estimate, thick bar: 50% credible interval, thin bar: 90% credible interval (CI) * 90%, ** 95%, *** 99% CI does not include 0. (**F**) Circle plot displays differentially expressed receptor ligand interactions between cell types (color) after *Alternaria* treatment. Squares denote significance (size) of up (black) or down (white) regulation after one dose (inner ring) or two doses (outer ring) of *Alternaria*.

Fig. 5. Mapping the unique subtypes of secretory epithelial cells in the nasal mucosa. (**A**) Density histograms show the posterior distribution from Bayesian Dirichlet Multinomial regression modeling (**Methods**) of log fold-change estimates (x axis) in proportions of (orange) and two (red) doses of *Alternaria* on the proportion of each immune cell type in the lymphoid (left) and myeloid (right) lineages. Black dot: point estimate, thick bar: 50% CI, thin bar: 90%

CI. * 90%, ** 95%, *** 99% CI does not include 0. (**B**) Heatmap shows the expression level (row-wise z-score of $\log_2$(TPM+1), color bar) of marker genes (right) specifically expressed (FDR<0.01) by each non-sensory epithelial subset (color bars). (**C-L**) Immunolocalization of epithelial cell subsets in the olfactory and respiratory nasal mucosa. (**C**) Cross section through the anterior section of the nose immunolabeled with OMP to delineate the olfactory epithelium in combination with Muc2 and GP2. Closeup of the olfactory epithelium (**D**, top inset of **C**) and respiratory epithelium (**E**, bottom inset of **C**) mucosa identifies the location of respiratory goblet cells marked by GP2 and sustentacular olfactory cells marked by Muc2. (**F)** Olfactory turbinates marked by OMP immunolabeled for DCLK1 in combination with Aquaporin 5. (**G**) Closeup of **F**. (**H**) Cross section through the posterior portion of the nose with olfactory turbinates (top), respiratory epithelium (bottom) and lateral nasal gland (lower right) demonstrating the distribution of Muc5b in the olfactory (labeled with OMP) and respiratory mucosa. (**I**) Closeup of olfactory epithelium and submucosa from **H**. (**J**) Closeup of respiratory mucosa of the nasal septum from **H** with epithelium overlying the submucosal glands. (**K**) Cross section through the anterior portion of the nose with septum on the right and lateral turbinates on the left demonstrating the expression of *Obp1a* mRNA detected by RNA scope ISH. (**L**) Closeup of *Obp1a* mRNA expression in the septal submucosal gland from K. (**M**) Density histograms show posterior distribution of log fold-change estimates in proportions of epithelial cell subsets after one (left) and two (right) doses of inhaled *Alternaria* allergens. Black dot: point estimate, thick bar: 50% CI, thin bar: 90% CI. * 90%, ** 95%, *** 99% CI does not include 0. (**N**) Volcano plot shows the relationship between $\log_2$ fold change (x axis) and significance (y axis) of differential expression of genes (points) within epithelial subsets (color legend) after one dose of *Alternaria*. (**O**) Lollipop plot shows the expression level (x-axis) of chitinase-like protein 4 (*Chil4*), before and after inhalation of *Alternaria* (color legend).

Fig. 6. Allergen-induced inflammation drives olfactory remodeling which is mediated by CysLTs derived from nasal tuft cells. (**A**) Estimated regression coefficients from Bayesian Dirichlet Multinomial regression (**Methods**) modeling the fold-change in proliferative state (x-axis) for each cell type (y-axis) after inhalation of Alternaria allergens in the olfactory (left) and respiratory (right) nasal mucosa. Black dot: point estimate, thick bar: 50% CI, thin bar: 90% CI. • 90%, ** 95%, *** 99% CI does not include 0 (**B**) Estimated proportion (y-axis) of proliferating HBCs (Methods) in each mouse (dots) naïve mucosa and after inhalation of Alternaria (x-axis). Bars show the mean and error bars show the S.E.M. (**C**) Scatter plots show low-dimensional PAGA embeddings of 17,318 olfactory epithelial cells (points) colored by cell-type cluster (left) and by pseudo-time coordinate (color legend, right). Trajectory (large points) and branches (color legend) were fit using elastic principal graphs. (**D**) Smoothed expression level (y-axis) of classical (*Krt5, Trp63, Kit, Ascl1, Omp, Tubb3*) and novel (*Tub1a, Tubb5, Stmn1*) markers of intermediate stages of neurogenesis (color legend) along the pseudo-time course (x-axis) from HBCs to mature OSNs. Stages (grey boxes) are shown as a visual guide. (**E**) Cross section through the posterior portion of the nose with olfactory turbinates stained with the novel ISN marker Stathmin-1 with close-up (top right inset). (**F**) IF stain of basal layer of olfactory epithelia from naïve (left) and after inhalation of one (center) and two (right) doses of *Alternaria*, showing Stathmin 1, Ki67 and keratin 5. (**G-H**) Representative scatter plots (**G**) and quantitation (**H**) show percentage of $EpCAM^+$ cells double-positive for Ki67 (x-axis) and keratin 5 (y-axis) using FACS of nasal mucosa in naïve (left) and *Alternaria*-treated (right) mice. p-values: Wald test. (**I-K**) A single dose of *Alternaria* was administered intranasally to $Chat^{Cre}Ltc4s^{fl/fl}$ and $Ltc4s^{fl/fl}$

mice, and the samples were collected on Day 3. (**I**) Cross-sections of olfactory turbinates stained with stathmin-1, Ki67, keratin 5 and Hoechst. (**J**- **K**) Representative images (**J**) and quantification (**K**) of Ki67-positive nuclei of basement membrane in olfactory turbinates. (**L**) Bar plots represent the quantitation of mix of basal and epithelial cells, defined as EpCAM^{intermediate} NCAM^{-} cells in WT, *Chat*^{Cre}*Ltc4s*$^{fl/fl}$ and *Pou2f*$^{-/--}$ mice 39 hours after a single dose of *Alternaria.* Data in **K** and **L** are means ± SEM, from three independent experiments, each dot represents a separate mouse. Mann-Whitney tests were used to determine significance in pairwise comparison of responses.

Figure 1

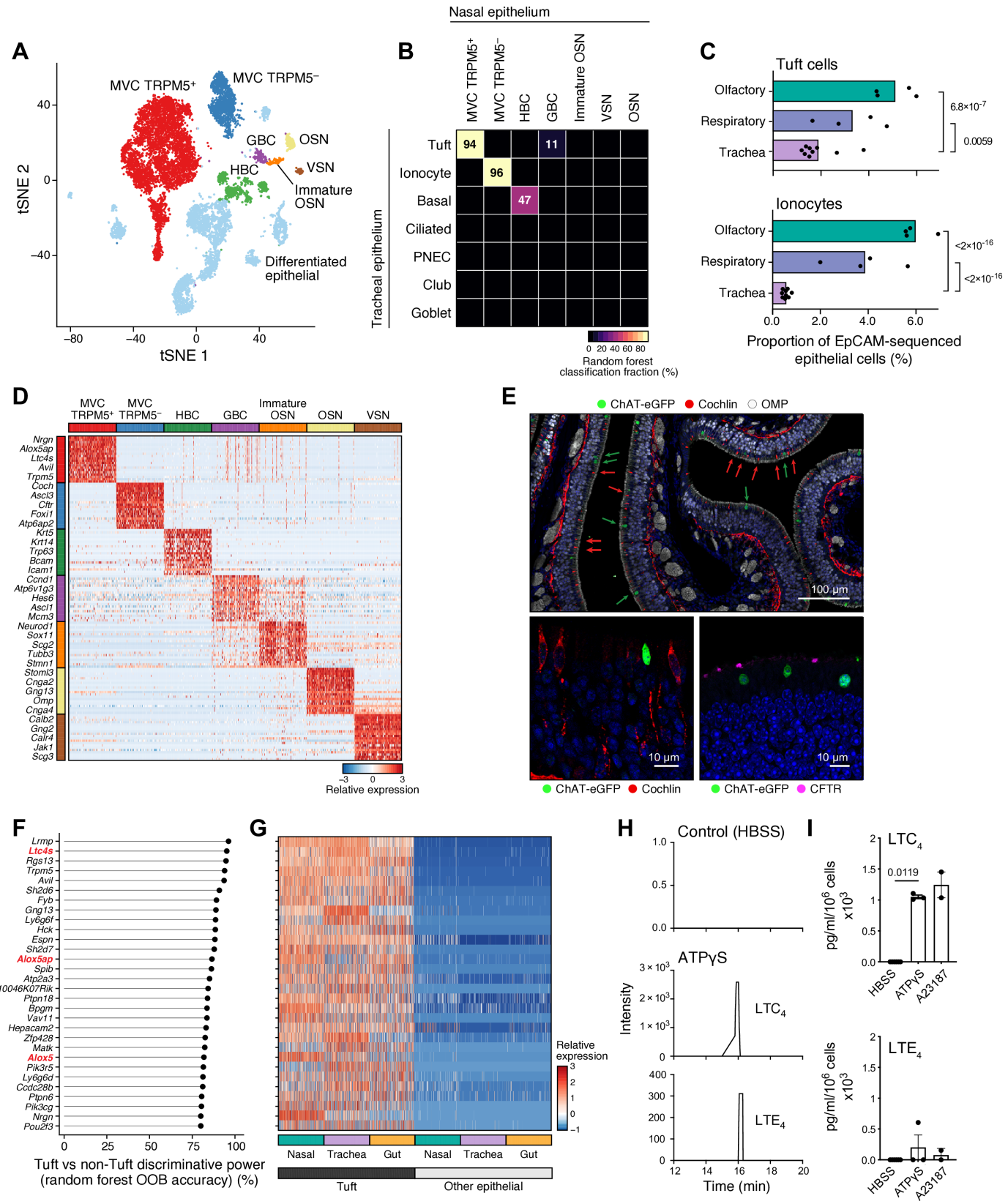
A
MVC TRPM5+
MVC TRPM5−
GBC
OSN
HBC
VSN
Immature OSN
Differentiated epithelial
tSNE 2
tSNE 1
B
Nasal epithelium
MVC TRPM5+
MVC TRPM5−
HBC
GBC
Immature OSN
VSN
OSN
Tracheal epithelium
Tuft
Ionocyte
Basal
Ciliated
PNEC
Club
Goblet
94
11
96
47
Random forest classification fraction (%)
C
Tuft cells
Olfactory
Respiratory
Trachea
6.8×10-7
0.0059
Ionocytes
<2×10-16
<2×10-16
Proportion of EpCAM-sequenced epithelial cells (%)
D
MVC TRPM5+
MVC TRPM5−
HBC
GBC
Immature OSN
OSN
VSN
Relative expression
E
ChAT-eGFP
Cochlin
OMP
100 µm
10 µm
CFTR
F
Tuft vs non-Tuft discriminative power (random forest OOB accuracy) (%)
G
Nasal
Trachea
Gut
Tuft
Other epithelial
Relative expression
H
Control (HBSS)
ATPγS
Intensity
LTC4
LTE4
Time (min)
I
LTC4
LTE4
pg/ml/10^6 cells x10^3
0.0119
HBSS
ATPγS
A23187

Figure 2

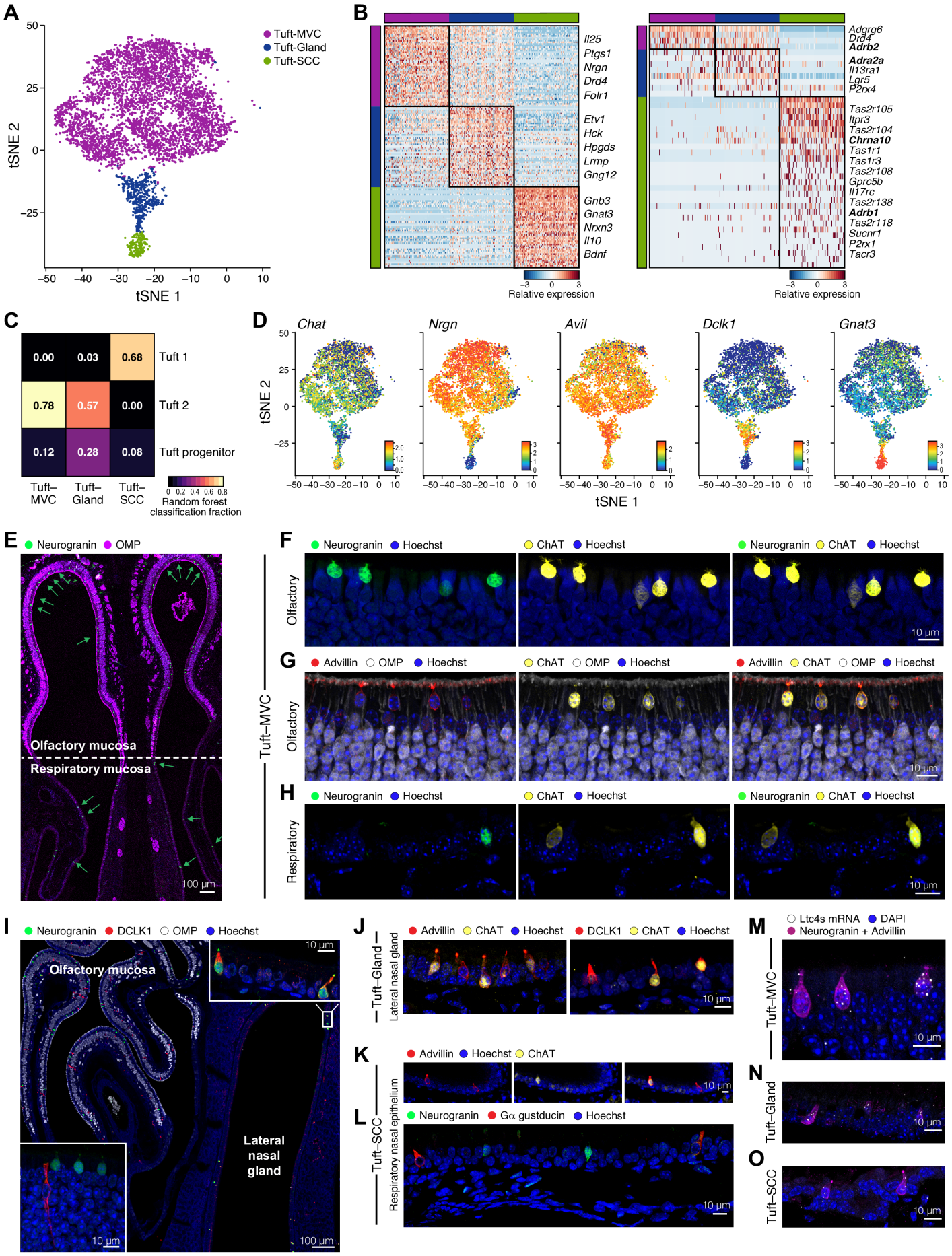
A
Tuft-MVC
Tuft-Gland
Tuft-SCC
tSNE 2
tSNE 1
B
Il25
Ptgs1
Nrgn
Drd4
Folr1
Etv1
Hck
Hpgds
Lrmp
Gng12
Gnb3
Gnat3
Nrxn3
Il10
Bdnf
Adgrg6
Drd4
Adrb2
Adra2a
Il13ra1
Lgr5
P2rx4
Tas2r105
Itpr3
Tas2r104
Chrna10
Tas1r1
Tas1r3
Tas2r108
Gprc5b
Il17rc
Tas2r138
Adrb1
Tas2r118
Sucnr1
P2rx1
Tacr3
Relative expression
C
Tuft 1
Tuft 2
Tuft progenitor
Tuft–MVC
Tuft–Gland
Tuft–SCC
Random forest classification fraction
D
Chat
Nrgn
Avil
Dclk1
Gnat3
tSNE 2
tSNE 1
E
Neurogranin
OMP
Olfactory mucosa
Respiratory mucosa
100 µm
F
Neurogranin
Hoechst
ChAT
Olfactory
10 µm
G
Advillin
OMP
Olfactory
H
Respiratory
Tuft–MVC
I
DCLK1
Olfactory mucosa
Lateral nasal gland
J
Tuft–Gland
Lateral nasal gland
K
L
Tuft–SCC
Respiratory nasal epithelium
Gα gustducin
M
Ltc4s mRNA
DAPI
Neurogranin + Advillin
N
O

Figure 3

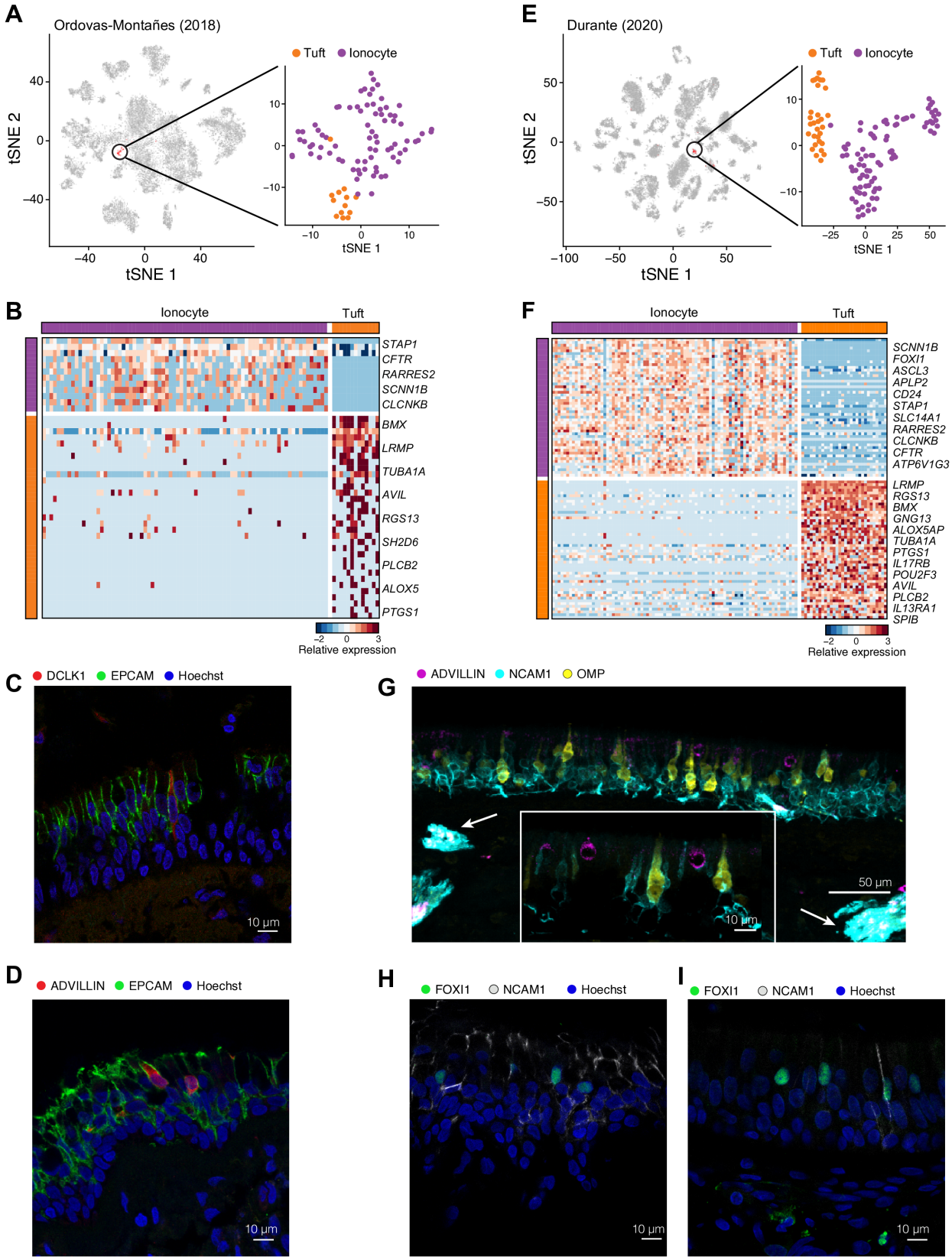
A
Ordovas-Montañes (2018)
Tuft
Ionocyte
tSNE 2
tSNE 1
E
Durante (2020)
Tuft
Ionocyte
tSNE 2
tSNE 1
B
Ionocyte
Tuft
STAP1
CFTR
RARRES2
SCNN1B
CLCNKB
BMX
LRMP
TUBA1A
AVIL
RGS13
SH2D6
PLCB2
ALOX5
PTGS1
Relative expression
F
Ionocyte
Tuft
SCNN1B
FOXI1
ASCL3
APLP2
CD24
STAP1
SLC14A1
RARRES2
CLCNKB
CFTR
ATP6V1G3
LRMP
RGS13
BMX
GNG13
ALOX5AP
TUBA1A
PTGS1
IL17RB
POU2F3
AVIL
PLCB2
IL13RA1
SPIB
Relative expression
C
DCLK1
EPCAM
Hoechst
10 µm
G
ADVILLIN
NCAM1
OMP
50 µm
10 µm
D
ADVILLIN
EPCAM
Hoechst
10 µm
H
FOXI1
NCAM1
Hoechst
10 µm
I
FOXI1
NCAM1
Hoechst
10 µm

Figure 4

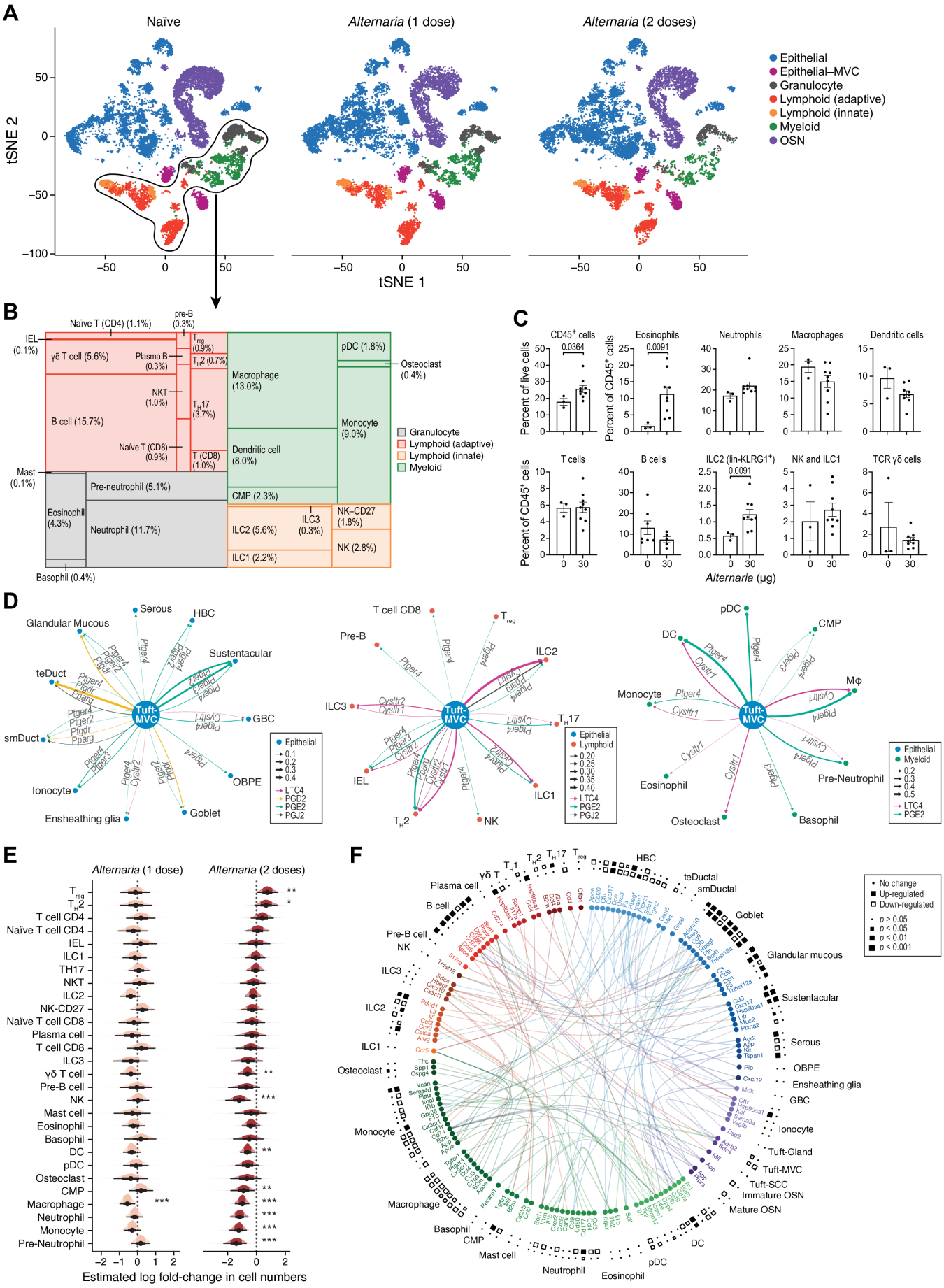
A
Naïve
Alternaria (1 dose)
Alternaria (2 doses)
tSNE 2
tSNE 1
Epithelial
Epithelial–MVC
Granulocyte
Lymphoid (adaptive)
Lymphoid (innate)
Myeloid
OSN
B
Naïve T (CD4) (1.1%)
pre-B (0.3%)
IEL (0.1%)
γδ T cell (5.6%)
Plasma B (0.3%)
Treg (0.9%)
TH2 (0.7%)
Macrophage (13.0%)
pDC (1.8%)
Osteoclast (0.4%)
NKT (1.0%)
TH17 (3.7%)
B cell (15.7%)
Monocyte (9.0%)
Naïve T (CD8) (0.9%)
T (CD8) (1.0%)
Dendritic cell (8.0%)
Mast (0.1%)
Pre-neutrophil (5.1%)
CMP (2.3%)
Eosinophil (4.3%)
Neutrophil (11.7%)
ILC3 (0.3%)
NK–CD27 (1.8%)
ILC2 (5.6%)
NK (2.8%)
ILC1 (2.2%)
Basophil (0.4%)
Granulocyte
Lymphoid (adaptive)
Lymphoid (innate)
Myeloid
C
CD45+ cells
Eosinophils
Neutrophils
Macrophages
Dendritic cells
T cells
B cells
ILC2 (lin-KLRG1+)
NK and ILC1
TCR γδ cells
Percent of live cells
Percent of CD45+ cells
Alternaria (μg)
D
Tuft-MVC
Serous
HBC
Glandular Mucous
Sustentacular
teDuct
GBC
smDuct
OBPE
Ionocyte
Goblet
Ensheathing glia
Epithelial
LTC4
PGD2
PGE2
PGJ2
T cell CD8
Treg
Pre-B
ILC2
ILC3
TH17
IEL
ILC1
TH2
NK
Epithelial
Lymphoid
pDC
CMP
DC
MΦ
Monocyte
Eosinophil
Pre-Neutrophil
Osteoclast
Basophil
Epithelial
Myeloid
LTC4
PGE2
E
Alternaria (1 dose)
Alternaria (2 doses)
Treg
TH2
T cell CD4
Naïve T cell CD4
IEL
ILC1
TH17
NKT
ILC2
NK-CD27
Naïve T cell CD8
Plasma cell
T cell CD8
ILC3
γδ T cell
Pre-B cell
NK
Mast cell
Eosinophil
Basophil
DC
pDC
Osteoclast
CMP
Macrophage
Neutrophil
Monocyte
Pre-Neutrophil
Estimated log fold-change in cell numbers
F
TH1
TH2
TH17
Treg
HBC
teDuctal
smDuctal
Goblet
Glandular mucous
Sustentacular
Serous
OBPE
Ensheathing glia
GBC
Ionocyte
Tuft-Gland
Tuft-MVC
Tuft-SCC
Immature OSN
Mature OSN
DC
pDC
Eosinophil
Neutrophil
Mast cell
CMP
Basophil
Macrophage
Monocyte
Osteoclast
ILC1
ILC2
ILC3
NK
Pre-B cell
B cell
Plasma cell
γδ T
No change
Up-regulated
Down-regulated
p > 0.05
p < 0.05
p < 0.01
p < 0.001

Figure 5

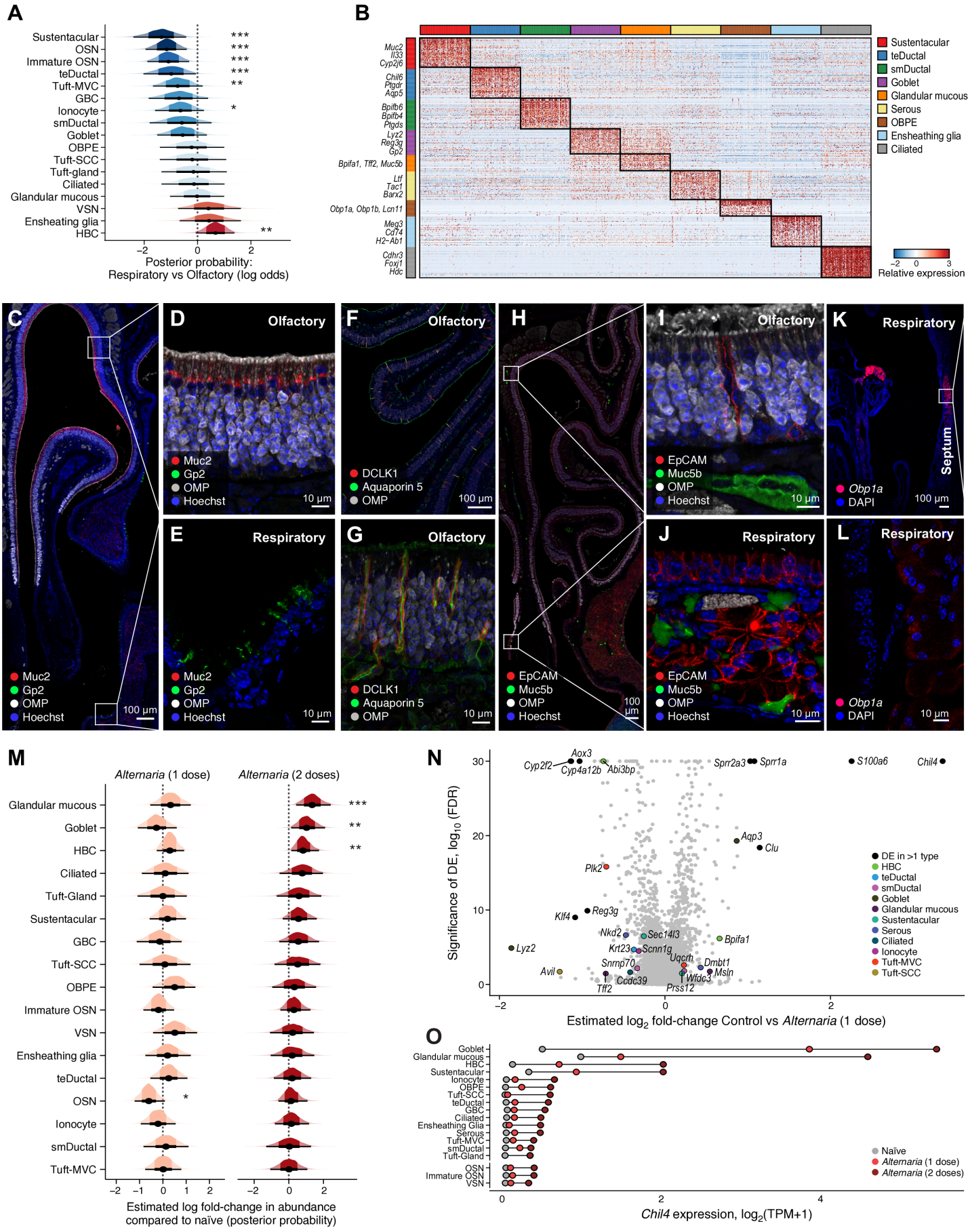
A
Sustentacular
OSN
Immature OSN
teDuctal
Tuft-MVC
GBC
Ionocyte
smDuctal
Goblet
OBPE
Tuft-SCC
Tuft-gland
Ciliated
Glandular mucous
VSN
Ensheating glia
HBC
Posterior probability:
Respiratory vs Olfactory (log odds)
B
Sustentacular
teDuctal
smDuctal
Goblet
Glandular mucous
Serous
OBPE
Ensheathing glia
Ciliated
Relative expression
C
D Olfactory
E Respiratory
F Olfactory
G Olfactory
H
I Olfactory
J Respiratory
K Respiratory
L Respiratory
Muc2
Gp2
OMP
Hoechst
DCLK1
Aquaporin 5
EpCAM
Muc5b
Obp1a
DAPI
Septum
10 µm
100 µm
M
Alternaria (1 dose)
Alternaria (2 doses)
Estimated log fold-change in abundance
compared to naïve (posterior probability)
N
Significance of DE, log10 (FDR)
Estimated log2 fold-change Control vs Alternaria (1 dose)
DE in >1 type
HBC
teDuctal
smDuctal
Goblet
Glandular mucous
Sustentacular
Serous
Ciliated
Ionocyte
Tuft-MVC
Tuft-SCC
O
Naïve
Alternaria (1 dose)
Alternaria (2 doses)
Chil4 expression, log2(TPM+1)

Figure 6

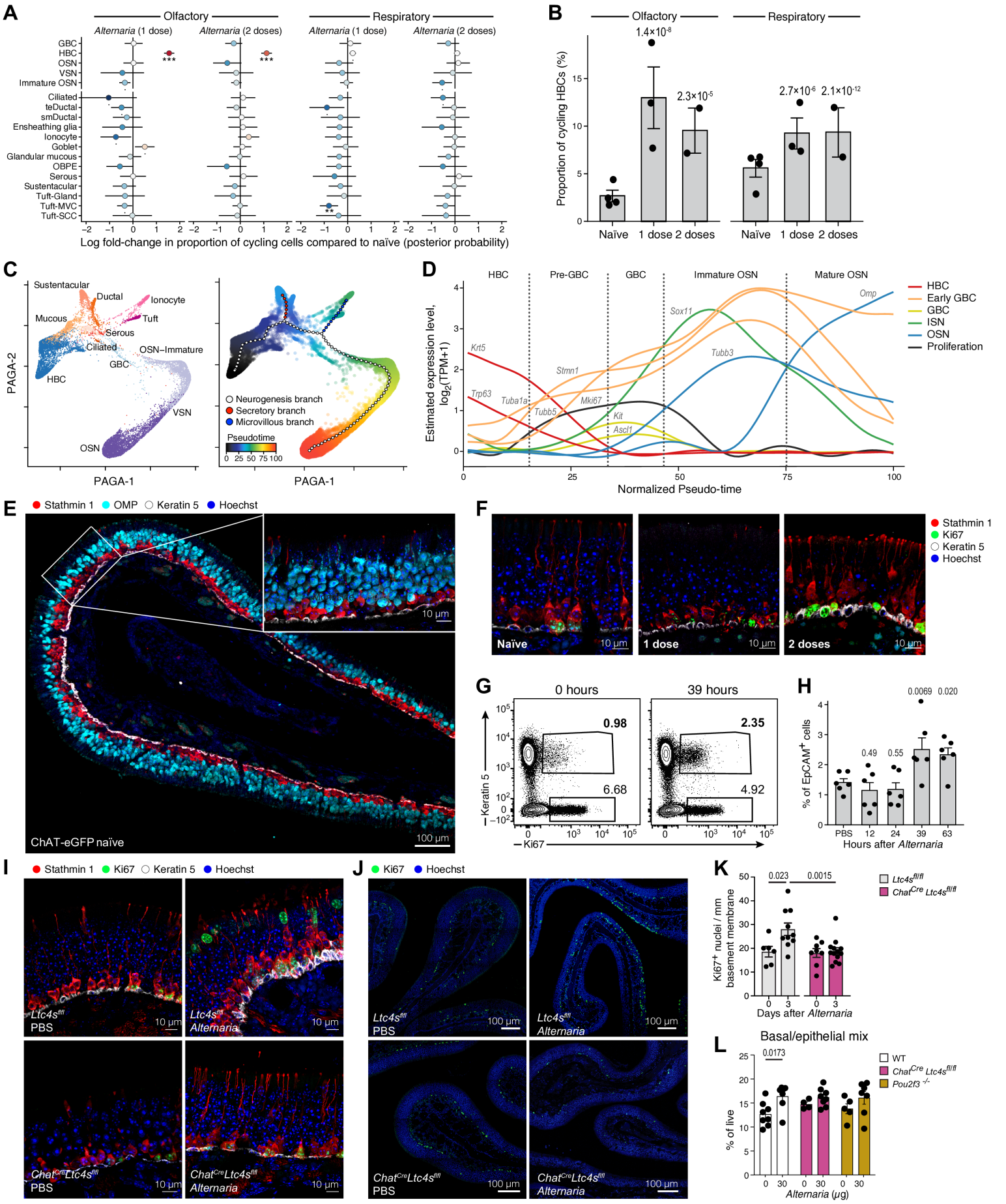
A
Olfactory
Respiratory
Alternaria (1 dose)
Alternaria (2 doses)
GBC
HBC
OSN
VSN
Immature OSN
Ciliated
teDuctal
smDuctal
Ensheathing glia
Ionocyte
Goblet
Glandular mucous
OBPE
Serous
Sustentacular
Tuft-Gland
Tuft-MVC
Tuft-SCC
Log fold-change in proportion of cycling cells compared to naïve (posterior probability)
B
Proportion of cycling HBCs (%)
1.4×10-8
2.3×10-5
2.7×10-6
2.1×10-12
Naïve
1 dose
2 doses
C
Sustentacular
Ductal
Ionocyte
Mucous
Tuft
Serous
Ciliated
OSN–Immature
GBC
HBC
VSN
OSN
PAGA-1
PAGA-2
Neurogenesis branch
Secretory branch
Microvillous branch
Pseudotime
D
HBC
Pre-GBC
GBC
Immature OSN
Mature OSN
Estimated expression level, log2(TPM+1)
Normalized Pseudo-time
Krt5
Trp63
Tuba1a
Tubb5
Stmn1
Mki67
Kit
Ascl1
Sox11
Tubb3
Omp
HBC
Early GBC
GBC
ISN
OSN
Proliferation
E
Stathmin 1
OMP
Keratin 5
Hoechst
10 µm
ChAT-eGFP naïve
100 µm
F
Stathmin 1
Ki67
Keratin 5
Hoechst
Naïve
1 dose
2 doses
10 µm
G
0 hours
39 hours
0.98
6.68
2.35
4.92
Keratin 5
Ki67
H
% of EpCAM+ cells
0.0069
0.020
0.49
0.55
PBS
12
24
39
63
Hours after Alternaria
I
Stathmin 1
Ki67
Keratin 5
Hoechst
Ltc4sfl/fl PBS
Ltc4sfl/fl Alternaria
ChatCreLtc4sfl/fl PBS
ChatCreLtc4sfl/fl Alternaria
10 µm
J
Ki67
Hoechst
Ltc4sfl/fl PBS
Ltc4sfl/fl Alternaria
ChatCreLtc4sfl/fl PBS
ChatCreLtc4sfl/fl Alternaria
100 µm
K
Ki67+ nuclei / mm basement membrane
0.023
0.0015
Ltc4sfl/fl
ChatCre Ltc4sfl/fl
Days after Alternaria
L
Basal/epithelial mix
0.0173
% of live
WT
ChatCre Ltc4sfl/fl
Pou2f3 -/-
Alternaria (µg)

Materials and Methods:

EXPERIMENTAL METHODS

Mouse models

Mice were maintained at the Brigham and Women's Hospital specific pathogen-free animal facility in accordance with the guidelines established by the Institutional Animal Care and Use Committee and Laboratory Animal Resource Center. The MGB Animal Care and Use Committee approved animal protocols in accordance with NIH guidelines. C57BL/6 wild type (WT) mice were purchased from Charles River Laboratories (Wilmington, MA) and ChAT^{BAC}-eGFP [B6.Cg-Tg(RP23–268 L19-EGFP)2Mik/J] (ChAT-eGFP) mice were purchased from Jackson Laboratories (Bar Harbor, ME)) and bred in house. *Ltc4s*$^{fl/fl}$ mice were provided by Dr. J. Boyce and generated by Ingenious targeting laboratory (Ronkonkoma, NY). ChAT-IRES-Cre [*Chat*$^{tm2(cre)Lowl}$] mice, purchased from Jackson Laboratories (Bar Harbor, ME) were mated to *Ltc4s* $^{fl/fl}$ mice to generate *Chat*^{Cre}*Ltc4s*$^{fl/fl}$. The mice used were between 11 and 36 weeks old. Pooled results include both male and female mice.

Aeroallergen Challenge Protocols

For all *in vivo* allergen challenge experiments, mice were given intranasal inhalations of *Alternaria alternata* culture filtrate after sedation with an intraperitoneal injection of ketamine (10 mg/kg) and xylazine (20 mg/kg) and euthanized with ketamine overdose. The *Alternaria* culture filtrate was administered at a dose of 30 µg per mouse in 20 µl of sterile phosphate-buffered saline (PBS). The intranasal instillation was administered either as a single drop at the middle of the nose or as two separate administrations of 10 µl per nostril.

Preparation of nasal cross sections

Snouts were collected from all mice after the mandibles and skin were removed. Snouts were immersed in 4% Paraformaldehyde (PFA) solution for 24 hours and then transferred to PBS. Fixed tissues were decalcified in 14% ethylenediaminetetraacetic acid (EDTA) for 14-24 days. Following decalcification, the nasal cavity was sectioned behind the incisors and in between the first three palatal ridges, yielding four coronal sections through the nasal cavity, and processed for routine paraffin embedding. Tissues were either frozen or embedded in paraffin. Paraffin embedded samples were sectioned to a thickness of 5 µm. Frozen samples were sections to thickness of 18 µm. Paraffin embedded sections were dewaxed in xylene for 20 minutes and hydrated through graded alcohols. The frozen sections were equilibrated to room temperature and post-fixed with methanol for 20 min.

Immunofluorescence staining of nasal cross sections

Heat-induced antigen retrieval was performed in either Target Retrieval solution (pH 6) (Dako) or in EDTA (pH 8.5) (Sigma) for 30-40 min. Slides were then blocked and permeabilized with a PBS-based solution containing 0.1% Triton X-100, 0.1% saponin, 3% bovine serum albumin, and 3% normal donkey normal donkey serum for 1 hour at room temperature. All samples were stained with primary antibodies overnight at 4°C, rinsed with with PBS with 0.1 % Triton-X (PSB-T) 3 times and incubated with secondary antibodies for 2 hours at room temperature unless otherwise indicated. The secondary antibodies included Alexa Fluor conjugates (488, 546, 594 and 647) (Invitrogen) (donkey anti-rat 594, donkey anti-mouse 594, donkey anti-mouse 488, donkey anti-goat 647, donkey anti-rabbit 546, donkey anti-rabbit 488, donkey anti-rabbit 647),

donkey anti-chicken FITC (Invitrogen), all used at a concentration of 4 μg/ml. Nuclear staining was performed with Hoechst 33342 nuclear stain (Sigma).

The following primary antibodies were used after performing antigen retrieval with Target Retrieval solution (pH 6) (Dako): rabbit anti-DCLK1 (Abcam, 5 μg/ml), chicken anti-GFP (Abcam, 35 μg/ml), rabbit anti-neurogranin (Sigma Millipore, 70 μg/ml), goat anti-OMP (WAKO, 1 μg/ml), rabbit anti-gustducin (Santa Cruz, 1 μg/ml), rat anti-cochlin (Sigma Millipore, 10 μg/ml), rabbit anti-Stathmin1 (Invitrogen, 5 μg/ml), rat anti-GP2 (MBL, 2.5 μg/ml), rabbit anti-aquaporin 4 (Sigma Millipore, 5 μg/ml), rabbit anti-aquaporin 5 (Sigma Millipore, 2 μg/ml), rabbit anti-Muc2 (Abcam, 1.25 μg/ml), mouse anti-Muc5b (Abcam, 5 μg/ml), mouse anti-GP2 (MBL), rabbit anti-cytokeratin-5 (APC-conjugated, Abcam, 1.6 μg/ml), rat anti-Ki-67 (Biolegend, 2.5 μg/ml), rat anti-EpCAM (Biolegend, 2.5 μg/ml). For samples stained with rat anti-Ki-67 antibody (Biolegend, 2.5 μg/ml) (**Fig.6G, I, G**), the heat-induced antigen retrieval was performed in Target Retrieval solution (pH 6) (Dako) for 1 hour, prior to blocking as described above. Heat antigen retrieval for samples co-stained with rabbit anti-advillin (Novus Biologicals, 1 μg/ml) and chicken anti-GFP (Abcam, 35 μg/ml) (**Fig.2G, J, K**) was performed in EDTA (pH 8.5) (Sigma) for 40 minutes.

For double labeling of coronal sections with two primary antibodies derived from the same species (rabbit), the samples were incubated with the first primary antibody (neurogranin or Gα gustducin) overnight. The first rabbit antibody immunoreactivity was then developed with a donkey anti-rabbit fluorophore conjugated antibody. Residual rabbit immunoreactivity was subsequently blocked overnight with unlabeled donkey anti-rabbit Fab fragment (AffiniPure Fab Fragment Donkey Anti-Rabbit IgG (Jackson ImmunoResearch, 26 μg/ml). Tissues were rinsed with PBS-T and incubated with the second primary antibody raised in rabbit (DCLK1 or neurogranin). After PBS-T rinse, the immunoreactivity of the second rabbit antibody was detected with donkey anti-rabbit antibody conjugated to a different fluorophore.

Goblet cell identification

Nasal tissue sections were also assessed by Periodic acid–Schiff (PAS) for identification of mucin-containing goblet cells. Slides were counterstained with hematoxylin for general morphologic examination.

CFTR staining with tyramide boost

For CFTR detection in cross sections, target retrieval was performed with a citrate buffer (Target Retrieval solution, pH 6, (Dako) for 30min after deparaffinization. The samples were blocked for 1 hour with 10% goat serum, then incubated overnight with a mix of primary antibodies, containing rabbit anti- CFTR (Alomone, 16 μg/ml) and chicken anti-GFP (Abcam, 35 μg/ml) at 4C. The slides were then treated with poly-HRP conjugated secondary antibody from Tyramide SuperBoost™ kit (Invitrogen) and the developed with tyramide working solution with Alexa Fluor 594 from Tyramide SuperBoost™ kit (Invitrogen) for 7 minutes. The reaction was terminated with the stopping solution provided in the kit and subsequently incubated with goat anti-chicken Alexa Fluor 488 conjugated antibody (Invitrogen, 4 μg/ml) and Hoechst for nuclear stain for 2 hours.

Images were acquired at the Brigham and Women's Hospital Confocal Microscopy Core Facility using the Zeiss LSM 800 with Airyscan confocal system on a Zeiss Axio Observer Z1

inverted microscope with 10× Zeiss [0.30 numerical aperture (NA)], 20× Zeiss (0.8 NA), and a 63× Zeiss oil (1.4 NA) objectives.

Imaging based quantitation of cell numbers

For quantitation of cell counts in cross sections, 4-5 representative images of respiratory mucosa were acquired, each area of 0.2- 1 mm^2. For estimating the frequency of neurogranin$^+$, Gα-gustducin$^+$ and double positive cells, individual cells were manually counted using ImageJ software (National Institute of Health, Bethesda, MD) and the length of basal membrane was measured in microns. For neurogranin and ChAT-eGFP or Gα-gustducin co-staining assessment, the images were collected as 3-11 representative images of olfactory and 3-5 images of respiratory epithelium, each area of 0.8-1 mm^2. To estimate the frequency of DCLK1-positive and neurogranin-positive cells in the lateral nasal gland (LNG), the length of basal membrane of LNG was measured in microns. The total number of ChAT-eGFP, neurogranin, Gα-gustducin, and Ki-67 immunoreactive cells in mouse nasal samples were manually counted using ImageJ software (National Institute of Health, Bethesda, MD).

For measurement of proliferating HBCs, Ki-67 positive cells were counted using the ImageJ software only at the basal membrane layer. Representative images (2-4 on average) of olfactory epithelium were collected for each sample, each image area of 0.07-0.15 mm^2 and Ki67 positive cells were evaluated against basement membrane length (mm). For assessment of OMP thickness, 2-3 representative images of olfactory turbinates with total area of 0.28 mm^2 were collected from ChAT-eGFP mice. To determine the thickness of olfactory mucosa, the area of the OMP$^+$ layer was measured in mm^2 using the ImageJ software.

In situ Hybridization (RNAscope)

The nasal snout for *in situ* hybridization was fixed in DEPC-treated 4% PFA and decalcified with DEPC-treated EDTA solution until sufficiently decalcified to section for OCT embedding. The tissue samples were sectioned at a thickness of 18 µms. For RNAscope *in situ* hybridization we used RNAscope® Fluorescent Multiplex Reagent Kit v2 (Cat No. 323120, Advanced Cell Diagnostics) assay following the manufacturer´s instructions. The nasal sections were post-fixed in 4% PFA for 15 min and then hydrogen peroxide for 10 min, both at room temperature. The sections were subsequently treated with Protease III for 10 min at 40°C before probe incubation. The probe to *Lct4s* was custom-made (Cat. No. 1092591-C1, Advanced Cell Diagnostics) and it targets exons 1-5 of the *Lct4s* transcript (nucleotides 98-534 of NM_008521.2). Expression of odorant binding protein 1a was evaluation using the mouse *Obp1a* probe (Cat. No. 500681, Advanced Cell Diagnostics). To mark tuft cells after *in situ* hybridization, sections were rinsed in PBS after final RNAscope wash and permeabilized and blocked again with 5% normal donkey serum/0.5% Triton X-100 Sorenson´s buffer and incubated with a mix of antibodies to neurogranin and advillin in a dilution of 1:100 over night at 4°C. After several washes with PBS, sections were incubated with a Donkey anti rabbit antibody coupled to Alexa Fluor 647 for 2 hours and mounted in DAPI-FluoromountG. After RNAscope and/or immunostaining, the sections were imaged on a Zeiss Axio Observer Z1 inverted microscope. The entire sections were imaged in consecutive z-slices separated by 0.21 µm using a 63x oil objective. The z stacks were then projected at maximum fluorescence intensity using ImageJ.

Whole septum imaging
For whole septum mount, the decalcified snouts were open longitudinally from the top to isolate the septum. The isolated septum was then permeabilized in the PBS-based solution described above for 3-4 hours. Primary chicken anti-GFP (Abcam, 35 µg/ml) antibody was added directly to the blocking buffer for incubation at 4°C for 72 to 96 hours. The specimens were then washed in PBS containing 0.1% Triton X-100 for 3 to 4 hours, and immunoreactivity to GFP was detected with secondary donkey anti-chicken secondary antibody, FITC (Invitrogen), applied for 72 hours at 4°C. Nuclear staining was performed with Hoechst 33342 nuclear stain (Sigma). The nasal septum was embedded using a glycerol-based mounting media and hardened under applied pressure, and 3-4 photographs of olfactory and respiratory epithelium, corresponding to 0.02-0.03 mm^2 of total area per septum, were obtained. The surface area of individual tuft cells was measured using ImageJ software (National Institute of Health, Bethesda, MD) and averaged per biological replicate. To calculate the frequency of tuft cells, the number of GFP^+ cells per image (ranging from 12 to 24 cells) was divided by the area captured in the focal plane.

Human sample immunohistochemistry
Subjects between the ages of 18 and 75 years were recruited from the Brigham and Women's Hospital (Boston, Mass) allergy and immunology clinics and otolaryngology clinics. The local institutional review board approved the study, and all subjects provided written informed consent. Ethmoid sinus tissue, middle or superior turbinate tissue was collected at the time of elective endoscopic sinus surgery from patients undergoing surgery for chronic rhinosinusitis or resection of pituitary adenoma. The samples were immediately placed in in RPMI medium (Corning, Corning, NY) with 10% FBS (ThermoFisher, Waltham, Mass) and 1 U/mL penicillin-streptomycin for transport to the laboratory on ice.

The samples were then fixed in 4% PFA for 4-8 hours and frozen in OCT for cryosectioning. The sections (6 µm) were post-fixed in methanol/acetone (1:1) mix for 15 min on ice. Heat-induced epitope retrieval was performed for 15 min in Target Retrieval solution (pH 6) (Dako) and all other steps were as described above for mouse snout processing. The primary antibodies included rabbit anti-advillin (Novus Biologicals, 1 µg/ml), mouse anti-NCAM (PE-conjugated, Biolegend, 0.4 µg/ml), goat anti-OMP (WAKO, 1 µg/ml), mouse anti-EpCAM (Santa Cruz,1 µg/ml) and rabbit anti-FOXI1 (ThermoFisher,0.5 µg/ml). The immunoreactivity was developed as described above with secondary antibodies raised in donkey.

Single-cell suspension preparation for FACS, ex vivo stimulation and RNA seq
To isolate respiratory epithelium from olfactory mucosa, the tissue overlying the proximal part of the nasal septal and lateral wall, together with vomeronasal organ, was separated from olfactory epithelium, covering the distal portions of nasal cavity. The isolated olfactory and respiratory mucosa were processed as described previously (96). The separated tissue including cartilages and bone fragments was first incubated in a PBS solution with dispase (16 U/ml) and deoxyribonuclease I (DNase I; 20 µg/ml) for 30 min at room temperature on a shaker at 120 rpm. The digestion was terminated by adding cold DMEM supplemented with 5% fetal bovine serum (FBS). Then, the nasal mucosa was separated from the bones mechanically and incubated in Tyrode's Solution with bicarbonate, HEPES, 0.25% BSA, without Ca^{2+} and added 31 U/ml of papain, 0.25 mg/ml L-cysteine and 20 µg/ml DNase I for 40 min at 37 °C on a rotating shaker at 220 rpm. The papain enzymatic activity was terminated with Tyrode's Solution with HEPES and Ca^{2+} and with 0.01 mg/ml leupeptin and the digested mucosa was triturated thoroughly and prepared for flow cytometric staining. All samples were pre-incubated with TruStain FcX™

(Biolegend) at 1µg per 10^6 cells in 100 µl volume for 10 minutes prior to immunostaining (**Fig. S1A**).

Single-cell suspensions from ChAT-eGFP mice were used for scRNA seq experiments at homoeostasis with specific enrichment of tuft cells (**Fig. 1** and **Fig. 2**) and after *Alternaria* inhalation without enrichment of tuft cells (**Fig. 4**, **5**, **6**). All samples from ChAT-eGFP mice were stained with monoclonal antibodies against CD45 and EpCAM, both at 25 µg per 10^6 cells in 100 µl volume for 40 min on ice. Propidium iodide (PI) was used as a dead cell exclusion marker and was added 1-3 minutes prior to sorting. To enrich for tuft cells, the epithelial cells from the respiratory and the olfactory mucosa were collected as three subsets of cells: globular tuft cells gated as $EpCAM^{high}$ $GFP^{+}FSC^{low}SSC^{low}$ cells, elongated tuft cells identified as $EpCAM^{high}$ $GFP^{+}FSC^{high}SSC^{high}$ cells, and other epithelial cells which were $EpCAM^{high}$ GFP^{-} (**Fig. S1B**, **C**). The experiment was performed twice on two separate days each with 2 male and 2 female mice.

For *Alternaria* remodeling experiments, the olfactory and respiratory epithelium were processed separately and $CD45^{+}$ and $EpCAM^{+}$ cells were sorted to represent 50% of cells in each location. The experiment was performed twice with the collected cells from olfactory mucosa of one mouse and respiratory mucosa from a different mouse of the opposite sex combined together to contribute equal proportions of a single sample. 6,000-10,000 cells per sample were collected into PBS and 0.04% (w/v) bovine serum albumin (BSA) and submitted for scRNA-seq (**Fig. 4-6**). Single-cell suspensions for low input (bulk) RNA-sequencing were derived from the whole nasal mucosa of *Ltc4s* $^{fl/fl}$ and *Chat*^{Cre}*Ltc4s* $^{fl/fl}$ mice. 1,000 $EpCAM^{intermediate}CD45^{-}FSC^{low}$ SSC^{low} cells (**Fig. S11B**) per sample were sorted into TCL buffer (Qiagen) supplemented with 1% 2-mercaptoethanol. The cells were derived from 6 mice of each genotype, from both male and female mice.

For evaluation of HBC proliferation, cell suspensions from the whole nasal mucosa were stained for extracellular markers with monoclonal antibodies against CD45, Kit (CD 117) and EpCAM, both at 25 µg per 10^6 cells in 100 µl volume for 40 min. The samples were incubated for 1 hour with fixation buffer from True-Nuclear™ Transcription Factor Buffer Set (Biolegend) and washed with permeabilization buffer from the same set. The samples were then stained with intracellular markers Keratin-5 (Abcam, 3.2 µg/ml) and Ki-67 (Invitrogen, 20 µg/ml) for 45-50 minutes. For detection of neuronal populations, the single cells suspensions were incubated at room temperature for 40 min with antibodies against NCAM1, CD45 and EpCAM at 25 µg per 10^6 cells in 100 µl volume.FACS was performed on BD LSR Fortessa™ Cell Analyzer.

Ex vivo stimulation of nasal tuft cells

Sorted $EpCAM^{high}GFP^{+}$ nasal tuft cells from the whole nasal mucosa of ChAT-eGFP mice were collected and then plated in DMEM-based media, containing DMEM/F-12, 5% Nu-Serum, 100 µg/ml Penicillin-Streptomycin and 0.25 µg/ml Amphotericin, at a concentration of 400,000 cells/ml and rested overnight. The cells were stimulated with 0.5 mM ATP-γ-S or 1µM A23187 in 50 µl of HBSS with Ca^{2+} and Mg^{2+} for 30 min. The supernatants were retained for ELISA and mass spectrometry assays (**Fig. 1**).

Lipid mediator detection.

PGD_2 and PGE_2 generation in the supernatants of stimulated tuft cells were measured by commercially available enzyme ELISAs from Cayman Chemical according to the manufacturer's instructions. The assays are based on competition between PGD_2/PGE_2 and

CysLT-acetylcholinesterase/ PGD_2-acetylcholinesterase/ PGE_2-acetylcholinesterase conjugate for a limited amount of PGD_2/PGE_2 ELISA Monoclonal Antibody. Targeted analysis for CysLTs was performed using liquid chromatography mass spectrometry at the Harvard Mass Spectrometry Facility using an ultimate 3000 LC coupled with a Q-exactive plus mass spectrometer (ThermoFisher). Briefly, proteins precipitation was performed by addition of methanol and incubating at -80 °C for 2 hours. The supernatants were dried under nitrogen flow and resuspended in methanol:mobile phase A 1:1. Cysteinyl Leukotriene HPLC Mixture I (Cayman Chemical) was used for preparation of an eight-level serial standard dilution in methanol. Ten microliters of samples were injected on a Kinetex C18 column (2.6u, 150x2.1 mm, Phenomenex), maintained at 30°C. The LC mobile phases were A: 10 mM ammonium Acetate, 0.1% Formic acid in water and B: Methanol, 0.2% formic acid. The gradient was as follow: starting at 20% B for 5 min, to 100% B in 10 min, followed by 10 min at 100%-, and 5-min re-equilibration at 20% B. the flow rate was maintained at 0.15 ml/min. The mass spec was set to positive polarity, with a resolution of 70000 and scanning mz 200 to 900. Compounds were quantified by integrating the area under the peaks of the compounds (extracted accurate mass at 5ppm, retention time confirmed by the authentic standards) and using the ratio with the IS to calculate the absolute concentration, using the calibration curve.

Droplet-Based Single-cell RNA-Sequencing (scRNAseq)

Sorted samples, containing 6,000-10,000 cells each, were submitted for droplet-based single-cell RNA-sequencing (10X Genomics) to the Single Cell Genomic Core at Brigham and Women's Hospital. Cells were washed and resuspended in PBS and 0.04% (w/v) bovine serum albumin (BSA) per the manufacturer's guidelines. Purified samples were run through 10X controller and individually bar-coded libraries were generated and pooled. Pooled library samples were sequenced on a Novoseq S1 (Illumina) in partnership with Dana Farber Cancer Institute (DFCI) Molecular Biology Core Facilities.

Low input RNA-sequencing

Cells from nasal single-cell suspensions were processed at the Broad Institute Technology Labs using low-input eukaryotic Smart-seq 2. Briefly, Smart-seq2 libraries were sequenced on an Illumina NextSeq500 using a High Output kit to generate 2 x 25 bp reads (plus dual index reads). Each sample's sequences were aligned utilizing STAR v2.4.2a (98) and the following parameters: --twopassMode Basic, -- alignIntronMax 1000000, --alignMatesGapMax 1000000, --sjdbScore 2, --quantMode TranscriptomeSAM, --sjdbOverhang 24. Alignments were processed using Picard v1.1073 tools to add read groups and other sequencing information, reorder the BAM file to the reference, and mark duplicate sequences. The data was assessed for quality using RNA-SeQC. RNA sequencing results were analyzed using R Bioconductor. Raw counts were generated using the FeatureCounts function of Rsubread. Raw input was used for normalization and differential expression analysis by DeSeq2 software. STAR aggregated mappings on a per-gene basis were used as raw input for normalization by DESeq2 software. Any genes with a mean normalized read count < 10 in any cell subset were removed from analysis. Genes were considered to be significantly differentially regulated based on a fold change in expression of > 2-fold and a false discovery rate of <0.05 based on a Benjamini-Hochberg adjusted p-value to correct for multiple comparisons.

COMPUTATIONAL METHODS

Pre-processing of scRNA-seq data.

Demultiplexing, alignment to the mm10 transcriptome and UMI-collapsing were performed using the CellRanger toolkit (version 1.0.1, 10X Genomics). For each cell, we quantified the number of genes for which at least one read was mapped, and then excluded all cells with fewer than 500 or greater than 6000. We also excluded cells in which the fraction of transcripts mapping to the mitochondrial genome was greater than 0.25. Expression values $E_{i,j}$ for gene i in cell j were calculated by dividing UMI count values for gene i by the sum of the UMI counts in cell j, to normalize for differences in coverage, and then multiplying by 10,000 to create TPM-like values, and finally calculating $\log_2$(TPM+1) values.

Variable gene selection.

A logistic regression was fit to the sample detection fraction, using the log of total number of UMIs for each gene as a predictor. Outliers from this curve are expressed in a lower fraction of samples than would be expected (deviance < -0.05 in all cases except -0.01 for myeloid and lymphoid cell clustering) given the total number of reads mapping to that gene, that is, they are specific to a cell-type, treatment, condition or state. The expression matrices were subset to these variable genes, and we normalized by dividing by the sum of transcripts in each cell to create $\log_2$(TP10K+1) values, which generated the digital gene expression (DGE) matrix that was used for all downstream analysis.

Dimensionality reduction by PCA and t-SNE.

We restricted the expression matrix to the subsets of variable genes and high-quality cells noted above, and values were centered and scaled before input to PCA, which was implemented using the R function 'RunPCA' included in the 'Seurat' package for RNA Sequencing analysis. Scores from these significant PCs were used as the input to further analysis. For visualization purposes only (and not for clustering), dimensionality was further reduced using the Barnes–Hut approximate version of *t*-SNE. This was implemented using the 'Rtsne' function from the 'Rtsne' R package using 5,000 iterations and a perplexity setting of 50. Scores from the first 25 principal components were used as the input to *t*-SNE in *Alternaria* and homeostasis datasets, for the lymphoid and myeloid cells the first 50 PCs were used.

K nearest-neighbor graph-based clustering.

To cluster single cells by their expression profiles we constructed a Shared Nearest Neighbor (SNN) Graph for our dataset using the built in Seurat function 'FindNeighbors'. The number k of nearest neighbors was set at 20, and the SNN was constructed using the first 25 principal components for homeostasis and *Alternaria* datasets. Once again for the immune cell subsets the first 50 PCs were used. We used this SNN Graph to identify clusters of cells using the Seurat 'FindClusters' function. We calculated clusters at several different resolutions to find one which could identify rare cell types with unique signatures. We used a resolution of 1.25 for the homeostasis and *Alternaria* datasets, we used resolutions of 1 and 3 for the myeloid and lymphoid subsets respectively. These resolutions identified rare cell types, but also split larger clusters of more common cells.

Cell type identification.
Because of the complexity and heterogeneity of the immune cells in our *Alternaria* dataset, we analyzed them separately after identifying them through an initial analysis of the entire dataset. The immune cells were identified using marker genes and further split into the myeloid and lymphoid lineage, and downstream analysis including final cell type identifications were made using these clusters. Detected clusters were mapped to cell types using known markers for nasal epithelial, immune, and neuronal subsets. Because of the large proportion of certain cell types, multiple clusters expressed high levels of markers for these types. Accordingly, we merged clusters expressing sets of known markers above a given threshold. These thresholds were variable between cell type gene sets. Gene sets used can be found in **Table S1**.

Excluding suspected doublets and low-quality cells.
Doublet clusters were identified through an initial clustering of the full datasets, and through subclustering of individual lineages and cell types. Clusters which co-expressed known markers for two distinct cell types, and which had elevated feature complexity relative to those cell types, were identified as doublets and removed. In total, 11 such clusters were identified in the *Alternaria* dataset, totaling 3429 cells. One further cluster of 614 cells was excluded based on high mitochondrial reads, and marker genes consisting predominantly of mitochondrial genes. In the homeostasis dataset 8 likely doublet clusters were identified and removed totaling 586 cells.

Testing for differential expression.
Differential expression (DE) tests were performed using MAST (97), which fits a hurdle model to the expression of each gene, consisting of logistic regression for the zero process (i.e., whether the gene is expressed) and linear regression for the continuous process (i.e., the expression level). All DE tests were run by comparing all cells of each type between conditions (downsampled to a maximum of 1,000 cells per condition). For each cell type, genes were only tested if they were detected in > 5 cells.

Construction of cell-type signatures.
To identify maximally specific genes for cell-types, we performed differential expression tests between each pair of clusters for all possible pairwise comparisons (downsampled to a maximum of 1,000 cells per group). Genes were tested if they were expressed in > 5 cells. Then, for a given cluster, putative signature genes were filtered using the maximum FDR Q value and ranked by the minimum $\log_2$ fold-change (across the comparisons). This is a stringent criterion because the minimum fold-change and maximum Q value represent the weakest effect size across all pairwise comparisons. Cell-type signature genes (**Table S2, S3, S6**) were obtained using maximum pairwise FDR=0.05 and a minimum $\log_2$ fold-change=0.1 in all cases except for lymphoid cell subtypes, where a more lenient cut-off of Fisher's combined FDR=0.0001 and minimum $\log_2$ fold-change=0.2 were used.

Scoring cells using signature gene sets.
To obtain a score for a specific gene set (length n) in a given cell, a 'background' gene set was defined to control for differences in sequencing coverage and library complexity. The background gene set was selected for similarity to the genes of interest in terms of expression level. Specifically, the $10n$ nearest neighbors in the 2D space defined by mean expression and detection frequency across all cells were selected. The signature score for that cell was then

defined as the mean expression of the *n* signature genes in that cell, minus the mean expression of the 10*n* background genes in that cell.

Mapping nasal cell-types to tracheal using supervised machine learning.
To compare nasal microvillous cells to recently characterized rare cell types in the trachea, we trained a random forest classifier using previously published single-cell profiles of tracheal epithelial cell types (22). The random forest was implemented using the "randomForest" R package. For training data we randomly sampled 250 cells per cell type, and used the 2000 most variable genes, the first 100 principal components, and 3 quality control metrics (number of genes detected, number of UMIs, and percent mitochondrial reads) as features. The model was then used to classify cells from the nasal dataset. Since some cell types would be exclusive to either nasal or tracheal epithelium and thus would not be expected to be correctly classified, we excluded low confidence predictions made by the model (with a classification probability < 0.5, computed as proportion of votes). A second random forest was fit in the same manner, this time using subtype-level classification of tuft cells (22), in order to identify subtypes of nasal microvillous cells.

Identification of human tuft cell subsets.
In the Durante (56) dataset the authors defined a subset of "Olfactory Microvillar Cells". We restricted our analysis to this subset and reanalyzed these cells to compare them to the nasal microvillar cells in the mouse. We identified variable genes and clustered cells using the methods described above and used a resolution of 0.25 for the final clustering which was then used for downstream analysis. Identification of DE marker genes was done using methods described above. Genes were tested if they were expressed in > 1 cell. For the Ordovas-Montañes dataset (53) no cluster of microvillar cells had been previously identified. We identified variable genes using a residual threshold of -0.001 and performed subsequent clustering and dimensionality reduction analysis using 50 principal components. Using a resolution of 3, we identified a cluster of 92 cells expressing known microvillous cell markers (*Foxi1*, *Cftr*, *Trpm5*). We then subset to this group and re-clustered it, identifying variable genes with a threshold of -0.01 and 5 principal components. Using a resolution of 1, we identified 6 clusters. One cluster expressed known tuft cell markers, and the remaining 5 expressed known ionocyte markers. We merged the Ionocyte expressing clusters and calculated marker genes with these two groups.

Estimation of bioactive lipid cell-type sources and sinks.
To infer lipid mediator production from single-cell data, we identified cell types expressing all genes required for the synthesis of a given lipid (**Table S5**), and visualized the proportion and mean expression of cells expressing all required genes using dot plots (**Fig. S5G**). Some lipids had multiple possible gene sets for their production, so a given cell only had to express one full set in order to be labelled as producing the lipid. To visualize the interactions between the novel tuft-MVC subset and its downstream targets, a directed graph was defined such that any cell-type where 10% of cells expressed an annotated receptor gene (at least one UMI), was connected with an edge. Graphs were visualized using the stress majorization algorithm (98).

Estimation of proportion of proliferating cells.
All cells were scored for a previously defined cell-cycle signature gene set defined from scRNA-seq data (99) as described above. To define a data driven threshold for cycling vs non-cycling cells, the distribution of scores was clustered into two groups using an unsupervised mixture of gaussians implemented using the Mclust package in R (100). The proportion of the cells in the high-expression cluster was reported as the proportion of proliferating cells.

Pseudo-time analysis of olfactory neurogenesis.
We isolated the 17,318 $CD45^-$ epithelial and neuronal cells (**Fig. 6C**, left) to examine the progression through neurogenesis using scanpy (101). The Partition-Based Graph Abstraction (PAGA) algorithm (90) was used to project cells into a low dimensional manifold, after defining unsupervised clusters generated using the Leiden algorithm (102). Elastic principal graphs (103) were then used to fit a branching tree through the PAGA co-ordinate space. Spurious single-node branches were removed, producing a tree with a main branch from HBCs to mature OSNs, and two branches which were interpreted as a secretory and microvillar cell branch (**Fig. 6C**, right), consistent with earlier lineage tracing data (3). The node within the HBC cluster was manually selected as the root node for pseudo-time calculation. Genes significantly varying along the pseudo-time path we identified by fitting generalized additive models (104) to the expression level of each gene (**Fig. S9D**). Genes were ranked by the pseudo-time coordinate of their first non-zero fitted value in order to identify early markers of neurogenesis (**Fig. S9E**).

Analysis of intercellular signaling networks.
To analyze cell-cell signaling in our dataset, we looked for the presence of a set of interactions from the combined CellPhoneDB (69) and FANTOM5 (70) interaction databases. In order to ensure that the interactions in these sets represented feasible cell-cell interactions, we used the Jensen COMPARTMENTS database (105), and subset our interaction table to just those interactions in which one interacting partner was extracellular with high confidence (> 4.5). For plotting purposes (**Fig. 4F**), we identified receptors or ligands differentially expressed after *Alternaria* treatment (FDR < 0.05 and $|\log_2$ fold-change$|$ > 0.1). We used the 5 most significantly differentially expressed genes per cell type. We further excluded genes with many interacting partner genes (≥10) as these were difficult to interpret and made visualization difficult. For each differentially expressed gene in an interaction, its interacting partner was displayed in the cell type in which it was most highly expressed. Circle plot visualization was produced using the 'edgebundleR' R package.

Bulk RNAseq pre-processing.
Computational pipelines for RNA seq analysis were implemented as described elsewhere (22, 23). Briefly, sequencer generated BCL files were converted to merged, de-multiplexed FASTQ files using the Illumina Bcl2Fastq software pack- age v.2.17.1.14. Paired-end reads were mapped to the UCSC mm10 mouse transcriptome using Bowtie57 with parameters '-q–phred33-quals -n 1 -e 99999999 -l 25 -I 1 -X 2000 -a -m 15 -S -p 6', which allows alignment of sequences with one mismatch. Gene expression levels were quantified as transcript-per-million (TPM) values by RSEM58 v.1.2.3 in paired-end mode (106).

Bulk RNAseq quality control.
Outlier analysis was performed using linear regression, fitted to an *Alternaria*-inducible gene expression score (top 20 differentially expressed genes in our scRNA-seq data). This procedure identified one mouse replicate which had a 'difference in fits' (DFFITS > 0.75), which was excluded from further analysis.

Deconvolution of cell type composition within bulk RNAseq profiles.
We determined the fraction of different cell types in each sample using CIBERSORTx (38) using default parameter settings. We provided our normalized $\log_2$(TPM+1) scRNA-seq data in (sub-sampled to a maximum of 200 cells per type) along with cell type cluster labels (**Fig. 4A, S5A, S5C, S7A**) as input to CIBERSORTx.

Testing for differences in cell proportions in bulk sequencing data.
To model the compositionality of cell type proportions either within single-cell data or CIBERSORTx estimates within prospectively isolated cell populations, a Bayesian Dirichlet Multinomial Mixture (DMM) model was fit using the "brms" package in R (107). In the *Alternaria* dataset cells from the epithelial and neuronal ($EpCAM^+$) and immune ($CD45^+$) compartments were collected separately. Cell proportions were therefore estimated as a fraction of their given compartment. The point estimates and posterior distributions for coefficients along with 50% and 90% credible intervals were then visualized as violin plots (**Fig. 4E, 5A, S6B**).